Bachelor Project

Czech
Technical
University
in Prague

F3 Faculty of Electrical Engineering
Department of Control Engineering

Autonomous vehicle traction system development

Ondřej Kuban

Supervisor: doc. Ing. Tomáš Haniš Ph.D.
January 2024

BACHELOR‘S THESIS ASSIGNMENT

I. Personal and study details

Student's name: **Kuban Ondřej** Personal ID number: **503163**

Faculty / Institute: **Faculty of Electrical Engineering**

Department / Institute: **Department of Control Engineering**

Study program: **Cybernetics and Robotics**

II. Bachelor’s thesis details

Bachelor’s thesis title in English:

Autonomous vehicle traction system development

Bachelor’s thesis title in Czech:

Vývoj trakčního systému autonomního vozu

Guidelines:

The primary goal of the thesis is to develop and implement autonomous vehicle path tracking, including traction control and torque vectoring functionality. The thesis will be done in cooperation with eForce formula student team will build on previously developed concept.
1. Get familiar with vehicle dynamics and traction control systems.
2. Implement and validate simulation framework for trajectory tracking and torque vectoring analysis.
3. Get familiar with vehicle lateral control based on anti-symmetrical torque distribution.
4. Develop and implement low-level traction system including torque vectoring system.
5. Develop and implement high-level path tracking system and integrate it with low-level one.
6. Evaluate developed systems.

Bibliography / sources:

[1] Dieter Schramm, Manfred Hiller, Roberto Bardini – Vehicle Dynamics – Duisburg 2014
[2] Hans B. Pacejka - Tire and Vehicle Dynamics – The Netherlands 2012
[3] Robert Bosch GmbH - Bosch automotive handbook - Plochingen, Germany : Robet Bosch GmbH ; Cambridge, Mass. : Bentley Publishers
[4] Rajamani R. (2012) Mean Value Modeling of SI and Diesel Engines. In: Vehicle Dynamics and Control. Mechanical Engineering Series. Springer, Boston, MA. https://doi.org/10.1007/978-1-4614-1433-9_9

Name and workplace of bachelor’s thesis supervisor:

doc. Ing. Tomáš Haniš, Ph.D. Department of Control Engineering FEE

Name and workplace of second bachelor’s thesis supervisor or consultant:

Date of bachelor’s thesis assignment: **25.08.2023** Deadline for bachelor thesis submission: **09.01.2024**

Assignment valid until:
by the end of summer semester 2023/2024

doc. Ing. Tomáš Haniš, Ph.D. Supervisor’s signature	prof. Ing. Michael Šebek, DrSc. Head of department’s signature	prof. Mgr. Petr Páta, Ph.D. Dean’s signature

III. Assignment receipt

The student acknowledges that the bachelor’s thesis is an individual work. The student must produce his thesis without the assistance of others, with the exception of provided consultations. Within the bachelor’s thesis, the author must state the names of consultants and include a list of references.

. _____
Date of assignment receipt

_____
Student’s signature

Acknowledgements

I express my gratitude to my supervisor, Doc. Ing. Tomáš Haniš, Ph.D., for his guidance and expertise while working on this thesis.
Additionally, I thank the team eForce Prague Formula for the opportunity to work on the autonomous driving systems. I would especially like to thank Vojtěch Michal and Marek Lászlo for sharing their knowledge of control engineering and vehicle dynamics.
I would like to express my gratitude to the team of Smart Driving Solutions for their helpfulness.
Lastly, special thanks belong to my parents for motivating and supporting me throughout my studies.

Declaration

I, Ondřej Kuban, declare that this thesis entitled 'Development of an Autonomous Vehicle Traction System' and the work presented in it are my own. I have cited all sources of information in accordance with the ethical principles for preparing university theses.

In Prague, January 9, 2024

.....

Abstract

This thesis focuses on developing, implementing, and validating algorithms for the autonomous formula developed by eForce Prague Formula student team, attempting the Formula Student competition. The aim is to improve the current systems of path-tracking and vehicle dynamics controls to increase the competitiveness of the team in the field of autonomous racing. The first part is dedicated to developing a twin-track mathematical model of the vehicle that enables a detailed analysis of the vehicle's behavior. The model assumes a planar motion of the vehicle and incorporates non-linear vehicle characteristics, such as tire modeling using equations derived by Hans B. Pacejka, to simulate the vehicle's behavior accurately. The following sections describe the path-tracking control algorithms and vehicle dynamics controls. The path-tracking algorithms use the key working principles of most path-tracking algorithms while incorporating different strategies. The vehicle dynamics controls consist of a cascade of controllers, with the lowest controller controlling the rotational speed of each wheel. Utilizing the relationship between wheel rotational speed and slip ratio, each wheel is controlled on slip ratio. Controllers that control the velocity and yaw rate of the vehicle are tuned with respect to the slip control. The final part of the thesis focuses on the validation of the developed control strategies and algorithms in the IPG Carmaker simulation environment.

Keywords: Twin-track model, vehicle dynamics control, traction control, antisymmetric torque distribution, path tracking, autonomous driving, control system design, Formula Student

Supervisor: doc. Ing. Tomáš Haniš Ph.D.
Prague 2, Karlovo náměstí, 13E

Abstrakt

Tato práce se zaměřuje na vývoj, implementaci a ověření algoritmů pro autonomní formuli vyvinutou týmem eForce Prague Formula, učastnící se závodů Formula Student. Cílem je vylepšit stávající systémy vedení po trati a řízení dynamiky vozu, a zvýšit tak konkurenceschopnost týmu v oblasti autonomního závodění.
První část je věnována vývoji dvoustopého matematického modelu vozidla, který umožňuje detailní analýzu chování vozidla. Model předpokládá rovinný pohyb vozidla a zahrnuje nelineární charakteristiky vozidla, například modelování pneumatik pomocí vztahů odvozených Hansem B. Pacejkou, aby bylo možné simulovat přesné chování vozidla.
Následující části popisují algoritmy řízení po trati a řízení dynamiky vozidla. Algoritmy vedení po trati využívají klíčové principy fungování většiny algoritmů vedení po trati, přičemž zahrnují odlišné strategie.
Řízení dynamiky vozidla se skládá z kaskády regulátorů, přičemž nejnižší regulátor řídí rychlost otáčení každého kola. Využitím vztahu mezi rychlostí otáčení kola a poměrem prokluzu, je každé kolo řízeno na prokluz. Regulátory, které řídí rychlost a rychlost otáčivého pohybu vozidla, jsou laděny s ohledem na řízení prokluzu.
Závěrečná část práce se zaměřuje na ověření navržených řídicích strategií a algoritmů v simulačním prostředí IPG Carmaker.

Klíčová slova: Dvoustopý model, kontrola dynamiky vozu, kontrola trakce, antisymetrické rozdělení kroutíciho momentu, vedení po trati, autonomní jízda,návrh řídích systémů, Formula Student

Překlad názvu: Vývoj trakčního systému autonomního vozu

Contents

1 Introduction 1
1.1 Motivation 1
1.2 Formula student 1
1.3 Autonomous system 3
1.4 State of the art 4
1.4.1 Path-tracking 4
1.4.2 Vehicle dynamics control 7
1.4.3 Torque vectoring 8

2 Vehicle platform 9
2.1 FSE.12 Formula student vehicle . 9
2.1.1 Powertrain 9
2.1.2 Steering actuator 10
2.1.3 Measurements 10
2.2 IPG Carmaker 11
2.2.1 FSE.12 CarMaker model 11

3 Vehicle Dynamics Modeling 13
3.1 Coordinate systems 13
3.2 Non-linear Twin Track Model . . 14
3.2.1 Wheel model 14
3.2.2 Tire model 15
3.2.3 Wheel and body projections . 16
3.2.4 Aerodynamics 18
3.2.5 Tire normal forces distribution 19
3.2.6 Vehicle dynamics 19
3.3 Control design models 20
3.3.1 Wheel speed controller design model 20
3.3.2 Body velocity controller design model 20
3.3.3 Yaw rate controller design model 20
3.3.4 Kinematic Model 21
3.4 Model verification 22
3.4.1 Powertrain 22
3.4.2 Drivetrain 22
3.4.3 Vehicle body 23
3.4.4 Model parameters 25

4 Path-tracking algorithms 27
4.1 Error calculation 28
4.2 Controllers 29
4.2.1 Heading controller 29
4.2.2 Cross-track controller 31

5 Vehicle dynamics control 33
5.1 Wheel speed controller 33
5.2 Slip ratio controller 35
5.3 Slip ratio distribution 36
5.4 Velocity controller 36
5.5 Yaw rate controller 38

6 Experiments 41
6.1 Vehicle dynamics control 41
6.1.1 Wheel speed controller 41
6.1.2 Slip ratio controller 43
6.1.3 Velocity controller 45
6.1.4 Yaw rate controller 46
6.2 Path tracking 51
6.2.1 U-Turn 52
6.2.2 Straight 54
6.2.3 S-Turn 56

7 Conclusion 59
7.1 Discussion 59
7.2 Future work 59

Bibliography 61

Figures

1.1 Formula student Germany team photo 2022[2] 1
1.2 Formula student skidpad track layout 2
1.3 Autonomous system architecture . 3
1.4 Illustration of pure pursuit algorithm [5] 6
1.5 Vehicle dynamics control systems diagram 7
1.6 ABS functionality illustration[7] . 7
1.7 ESC functionality illustration[9] . 8

2.1 FSE.12 Formula student vehicle . 9
2.2 Motor assembly 10
2.3 INS Ellipse2-D 10
2.4 CarMaker eForce formula 3D visualisation 11

3.1 Vehicle body coordinate system . 13
3.2 Architecture of non-linear twin-track model 14
3.3 Wheel coordinate system [18] . . . 15
3.4 Tire model 16
3.5 Top view of vehicle model 17
3.6 Electric powertrain dynamics . . . 22
3.7 Wheel speed torque step response 23
3.8 Vehicle speed torque step response 23
3.9 Vehicle body motion validation . 24

4.1 Path-tracking architecture 27
4.2 Shadow vehicle illustration 29
4.3 Yaw controller design 30
4.4 Heading controller step response for multiple velocities 30
4.5 Cross-track controller root locus 31
4.6 Cross-track controller step response for multiple speeds 32

5.1 Low-level control system architecture 33
5.2 Pole position based on the wheel speed v_x^w 34
5.3 Root locus of system with controller for 2 m/s 35
5.4 Fitted curves for proportional and integral gains 35
5.5 Wheel speed controller scheme . 35
5.6 Slip ratio distribution scheme . . 36
5.7 Velocity controller design 37
5.8 Velocity controller step response for various velocites 38
5.9 Velocity controller effort step response for various velocites 38
5.10 Root locus of yaw rate controller 39
5.11 Yaw rate controller step response for various velocites 40
5.12 Yaw rate controller step response for various velocites 40

6.1 Wheel speed step response at 5 m/s 41
6.2 Wheel speed step response at 15 m/s 42
6.3 Wheel speed step response at 30 m/s 42
6.4 Front left slip ratio controller response 43
6.5 Rear left slip ratio controller response 44
6.6 Slip ratio controller μ jump test 44
6.7 Velocity controller step response 45
6.8 Velocity controller step response effort 45
6.9 Velocity controller step response with μ jump 46
6.10 Velocity controller step response effort with μ jump 46
6.11 Verification model 10 degrees steering sine wave maneuver at 10 m/s 47
6.12 Design model 10 degrees steering sine wave maneuver at 10 m/s 47
6.13 Verification model 5 degrees steering sine wave maneuver at 25 m/s 48
6.14 Design model 5 degrees steering sine wave maneuver at 25 m/s 48
6.15 Verification model 5 degrees steering angle step response with 0.6 μ split 49
6.16 Verification model ramp steer response at 10 m/s 49
6.17 Verification model ramp steer response at 20 m/s 50

Tables

3.1 Table of vehicle parameters 25
3.2 Table of aerofoil parameters 25
3.3 Table of Pacejka magic formula parameters 25

6.18 Path configurations 51
6.19 S-turn path 51
6.20 U-turn of 20 m diameter at velocities of 5, 10 and 13 m/s 52
6.21 U-turn of 20 m diameter reference heading tracking 52
6.22 U-turn of 20 m diameter cross track error 53
6.23 U-turn of 20 m diameter steering command 53
6.24 U-turn of 10 m diameter at a velocity of 7 m/s 54
6.25 U-turn of 10 m diameter cross track error 54
6.26 Straight path manuever 55
6.27 Straight path cross track error . 55
6.28 S-turn of 16.25 m diameter at a velocity of 5 and 10 m/s 56
6.29 S-turn of 16.25 m diameter reference heading tracking 56
6.30 S-turn of 16.25 m diameter cross track error 57
6.31 S-turn of 16.25 m diameter steering command 57

Chapter 1

Introduction

1.1 Motivation

Since 2019, Team eForce Prague Formula, operating under the Czech Technical University in Prague, has participated in the Formula Student Driverless competition. The team's primary objective is to develop, test, and validate autonomous racing algorithms deployed in competitions worldwide. As the team's proficiency in autonomous driving technology advances, the need for algorithms with higher functionality grows. To this point, there has been little emphasis on vehicle dynamics control, an area that offers potential for additional research and advancement.

1.2 Formula student

Formula Student [1] is an international competition between universities from all around the world. The competition focuses on building small formula-like vehicles.

Figure 1.1: Formula student Germany team photo 2022[2]

In the year 2019, Formula Student introduced the driverless category. The competition itself has static and dynamic disciplines, where the static disciplines focus on the car design, its evaluation, and safety.
On the dynamic disciplines, the car is placed in the start area of the designated track. The track is marked with blue, yellow, and orange cones, where blue and yellow cones represent the track itself, and the orange cones usually define the start and finish area. There are four dynamic disciplines: Acceleration, Skidpad, Autocross, and Trackdrive. Disciplines are designed to test various capabilities of the car and its autonomous systems.
Acceleration is a discipline that assesses the maximal speed and acceleration of a vehicle, comprising a straight section of 75 meters with an additional 75 meters reserved for braking. While the track width may change, it remains consistent for each run, measuring at least 3 meters wide.
The skidpad is an eight-shaped track, as visible in Figure 1.2, with a width of 3 meters. The car begins in the starting area and moves through two right-hand turns, progressing to two left-hand turns before completing the course with a straight driving section to the finish area. The skidpad evaluates a vehicle's capacity to withstand high lateral forces experienced during high-speed circular driving.
The autocross course ranges from about 200 to 500 meters in length and con-

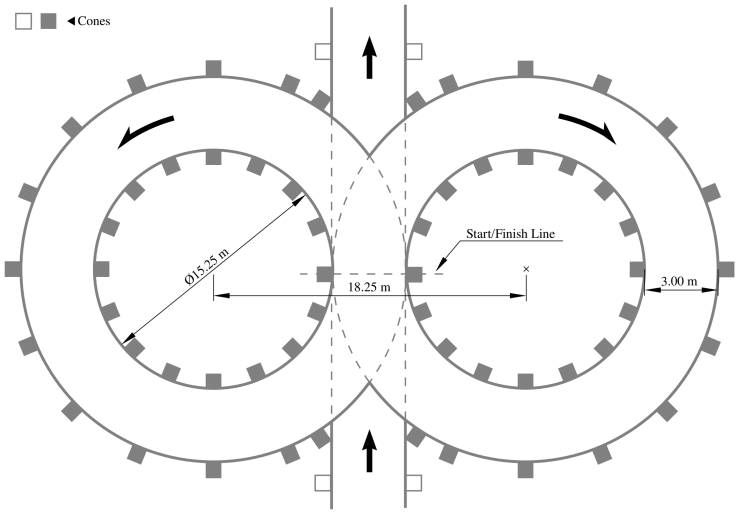

Figure 1.2: Formula student skidpad track layout

sists of straights, lengthy curves, and hairpins. The minimum width measures 3 meters, while the stretches of straight track do not exceed 80 meters. The radius of a steady turn can be as large as 50 meters, while hairpins feature a minimum outside diameter of 9 meters. The course layout changes for each competition, and the car receives no advance information on the track's configuration. The Trackdrive discipline is comparable to Autocross, with the exception that in Trackdrive, the car completes ten laps instead of one. These disciplines aim to test the dynamic capability of the car by subjecting

it to diverse scenarios that were not evaluated in preceding disciplines. The autonomous formulas typically achieve speeds greater than 5m/s in all of these disciplines.
The competition releases its own rules annually, with a primary emphasis on the safety of the car and operator. One rule states that if the formula exceeds the track boundary with all four wheels, it must be remotely stopped, resulting in a *Did Not Finish* status for the run.

1.3 Autonomous system

The autonomous system is responsible for all high-level functionality necessary for driverless operation, including localization and mapping, path planning, data processing, machine vision, and path tracking, as well as vehicle dynamics handling. The autonomous pipeline diagram 1.3 details various components of the system. Blue boxes denote units that manage the car's low-level system, such as the battery management system, inverters, steering actuator, and more. The yellow boxes represent the nodes that exist within the autonomous system, with each node serving a distinct purpose. The vision node uses a neural network to process images from the stereocamera and detect cones. The CAN1, CAN2, and STEERING CONTROL nodes are responsible for

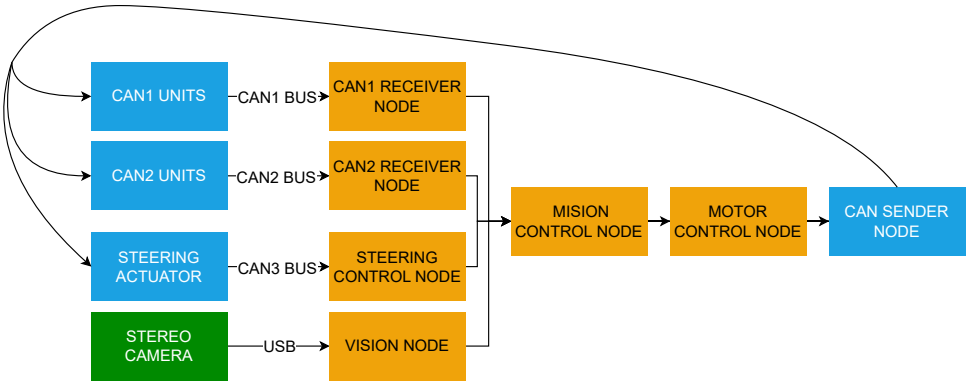

Figure 1.3: Autonomous system architecture

transforming data from the CAN bus network into a format that is more suited to the autonomous system. CAN1 is reserved for high-priority systems, such as motor inverters and batteries. CAN2 is primarily used for collecting data from auxiliary sensors. The processed data from the CAN bus and cone detections are then sent via internode communication to the mission control node. The mission control node is responsible for localizing and mapping the track, as well as path planning, path tracking, and calculating speed for each part of the track. Commands from the mission node are then sent to the motor control node, which controls the vehicle dynamics. Finally, all of the data are sent to the system.

1.4 State of the art

1.4.1 Path-tracking

Autonomous driving technology revolves around three key components: neural networks that interpret the surrounding environment, planning algorithms that chart the vehicle's course, and path-tracking algorithms. The planning algorithms are designed to chart a feasible path that is clear of obstacles and minor road issues. For consumer vehicles, navigation involves avoiding common obstacles such as potholes and puddles. The vehicle's navigation system relies on a combination of pre-loaded map data and real-time inputs from its perception systems.

Path-tracking algorithms are utilized to control the steering of the wheels to guarantee that the vehicle follows the planned route. These algorithms rely on various data inputs, such as the precise location of the vehicle, its speed, orientation, and sensor feedback on wheel angles. The key operating principle of the path-tracking algorithms is to adjust the steering based on updates from the sensors, ensuring that the vehicle closely follows the intended trajectory in a dynamically changing environment. The following algorithms are commonly used.

Model predictive control

The Model Predictive Controller (MPC)[3] can utilize linear or non-linear vehicle models to determine the optimal control action. While many implementations use the kinematic model, more complex models that consider tire characteristics and other vehicle features can also be employed. However, with increased complexity comes longer calculation times. The model is defined as a state-space model 1.1, with some initial state x_0,u_0,y_0, while limiting the optimization problem with the conditions 1.2, 1.3, 1.4.

$$\begin{aligned} x_{k+1} &= Ax_k + Bu_k \\ y_k &= Cx_k + Du_k && (1.1) \\ u_k &\leq u_{max} && (1.2) \\ x_{min} \leq x_k &\leq x_{max} && (1.3) \\ y_{min} \leq y_k &\leq y_{max} && (1.4) \end{aligned}$$

Model predictive control utilizes a cost function J_k 1.5 that needs to be minimized, while the optimization problem is done on a finite time horizon. This cost function is defined as follows:

$$J_k = x_{k+N}^T P x_{k+N} + \sum_{i=0}^{N-1} (x_{k+i}^T Q x_{k+i} + u_{k+i} R u_{k+i}) \tag{1.5}$$

The equation defines the length of the prediction horizon as N, with x_{k+i} and u_{k+i} representing the state and input vectors at future time step $k+$

i, respectively. Q and R are weighting matrices used to determine the importance between the states and control actions, tuning the system control behavior. The use of these matrices can be adjusted to, for example, place more emphasis on the total energy used. Finally, the P matrix determines the terminal state of the system by setting the desired state at the end of the prediction horizon.

Stanley controller

The Stanley controller [4] is a non-linear control system known for its robustness and relatively modest computational power requirements. It was originally developed for a rally car competing in the DARPA Grand Challenge 2005, where it demonstrated its effectiveness and reliability. The controller manages both the speed and steering angles of a vehicle, with the steering angle aspect responsible for path tracking. The Stanley controller uses the front axle as its reference coordinate system, which means that all control errors are measured in relation to this point. The Stanley control law is, as described in the equation for the steering control.

$$\delta(t) = (\psi(t) - \psi_{ss}(t)) + \arctan \frac{k_{\perp} e_{\perp}(t)}{k_{soft} + v(t)} \tag{1.6}$$

$$+ k_{d,yaw}(\dot{\psi}_{meas} - \dot{\psi}_{traj}) + k_{d,steer}(\delta_{meas}(i) - \delta_{meas}(i+1)) \tag{1.7}$$

The equation includes a member, $\delta_{meas}(i) - \delta_{meas}(i+1)$ that compensates for the delay and overshoot of the steering controller. The $\delta_{meas}(i)$, $\delta_{meas}(i+1)$ is the measured steering angle at discrete sample indexes i, $i+1$, the $k_{d,steer}$ is the gain of this member. The $k_{d,yaw}(\dot{\psi}_{meas} - \dot{\psi}_{traj})$ acts as a damping part of the controller that damps the yaw rate of the vehicle, $\dot{\psi}_{meas}$ is the measured yaw rate, $\dot{\psi}_{traj}$ is the desired yaw rate defined by the trajectory and $k_{d,yaw}$ is the gain parameter. In the equation $\arctan \frac{k_{\perp} e_{\perp}(t)}{k_{soft}+v(t)}$, $e_{\perp}(t)$ stands for cross track error, where $k_{\perp}$ is its gain. this member of the Stanley controller controls the distance divination from the track. The output of this member depends on velocity $v(t)$, resulting in less aggressive behavior at higher speeds. The k_{soft} parameter ensures the controller is not too aggressive for lower speeds. Lastly, the $\psi(t) - \psi_{ss}(t)$ controls the heading divination from the reference. Where $\psi(t)$ is the measured heading in the global coordinate system and $\psi_{ss}(t)$ is the reference heading of the trajectory.

Pure pursuit controller

The pure pursuit controller is a simple path-tracking controller. The controller aims to reach the point on the path within the lookahead distance d_{LA}. To achieve this, the control action utilizes the kinematic model to calculate the necessary action.

$$\delta = \arctan\left(\frac{2L\sin(\alpha)}{d_{LA}}\right) \tag{1.8}$$

In this equation, the length of the vehicle is represented by L, while α denotes the angle between the vehicle heading and the lookahead point. The equation for the control action is illustrated in Figure 1.4. Keeping the lookahead

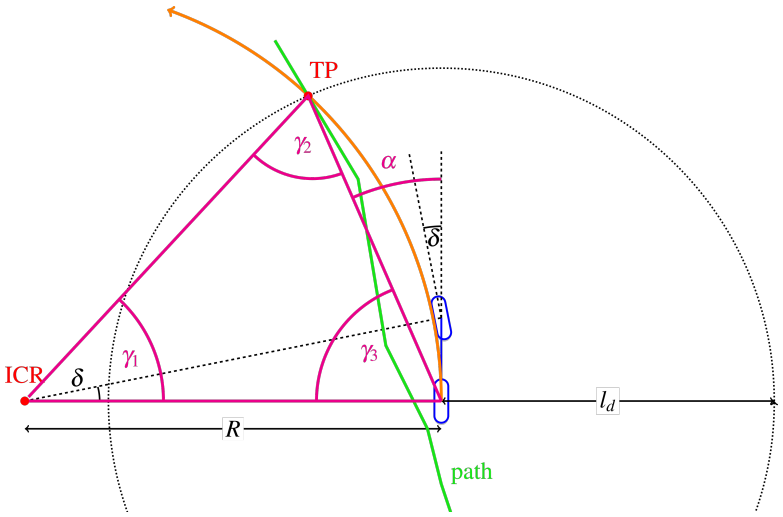

Figure 1.4: Illustration of pure pursuit algorithm [5]

distance d_{LA} constant can result in unstable behavior at various speeds. Therefore, the lookahead distance is often parameterized by velocity, as described by the following equation.

$$d_{LA} = K_{LA} v \tag{1.9}$$

The parameter K_{LA} is used to tune the controller behavior for a given vehicle velocity v.

1.4.2 Vehicle dynamics control

Modern vehicle systems, such as anti-lock brake system (ABS)[6], traction control system (TCS)[10], and electronic stability control (ESC)[8], have made cars safer, easier to control, and more efficient. These systems were initially implemented on combustion vehicles, where the engine is not particularly fast, effective, or precise. Systems that were mostly developed for combustion engines have been transferred to vehicles with electric powertrains, where speed and accuracy are among the main advantages. These systems can be divided into four groups as shown in figure 1.5, systems that work with controlling the brakes, and systems working with engine.

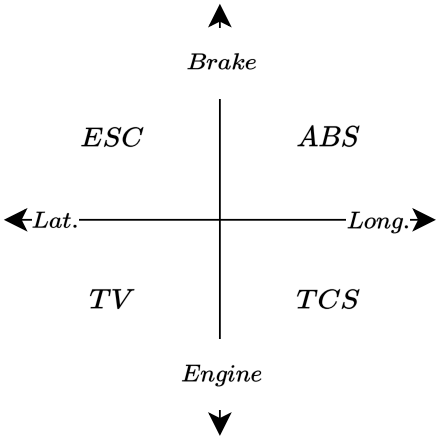

Figure 1.5: Vehicle dynamics control systems diagram

Anti-lock brake system

The car's behavior remains unaffected by the active brake system, and the driver retains full control upon brake activation. The ABS limits the brake force applied to each wheel and monitors their rotational speed. If a tire is detected as locked, meaning its rotational speed is near zero, the system decreases the hydraulic brake pressure to allow the wheel to start spinning again. Normally, when a car skids, it can go into an understeer or oversteer skid. However, with ABS active, the driver can regain partial control over the vehicle, as can be seen in figure 1.6.

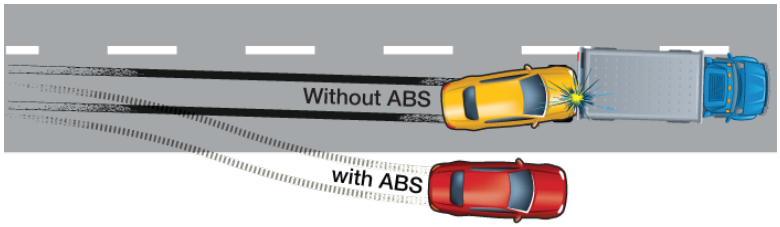

Figure 1.6: ABS functionality illustration[7]

Traction control system

The TCS, like the ABS, monitors the rotational speed of the wheels and detects rapid changes in that speed. This behavior indicates that the car is generating more force than the tire characteristics can handle, resulting in the vehicle becoming hard to control or even uncontrollable. To prevent wheel slip, the TCS controls the engine speed, and therefore the wheel speed, which in turn controls slip on these wheels. Advanced versions of traction control utilize the active differential. On four-motor electric vehicles, each motor is controlled individually.

Electronic stability control

The ESC is the superior system to the ABS, it monitors the vehicle's yaw rate and steering angle to assist the driver in scenarios where braking and steering occur simultaneously, such as highway collision avoidance. In such cases, the ESC uses the lower system to prevent high slips and controls the brake forces on each individual wheel to steer the car in the intended direction. Figure 1.7 illustrates the behavior of car with and without ESC.

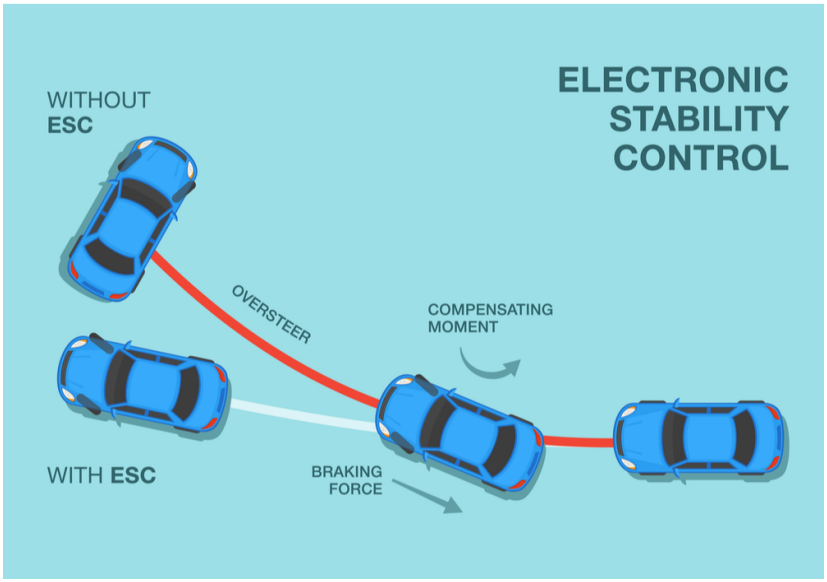

Figure 1.7: ESC functionality illustration[9]

1.4.3 Torque vectoring

A more advanced system, torque vectoring (TV), is based on ESC and effectively uses TCS. Similar to ESC, torque vectoring monitors the vehicle's yaw motion and steering angle, and controls each wheel of the vehicle to match the desired behavior. The system allows the driver to adjust the vehicle's behavior, such as increasing oversteer, and then controls each wheel accordingly, as stated by Rimac Bugatti. [11].

Chapter 2

Vehicle platform

Figure 2.1: FSE.12 Formula student vehicle

2.1 FSE.12 Formula student vehicle

The FSE.12 formula car has several distinctive features, such as a custom aerodynamic package, suspension system, and a carbon fiber chassis. It is powered by a 600V battery with a 7.45 kWh capacity. Additionally, each wheel of the car is equipped with its own electric motor. The car's design maintains a relatively light weight of 201 kg, while its dimensions measure 1.2 meters in width and 2 meters in length, contributing to its maneuverability.

2.1.1 Powertrain

Each motor of the vehicle can produce 35.37 kW of power and 29.1 Nm of peak torque, with a maximum speed of 20,000 rpm. The torque from each motor is amplified through a planetary gearbox with a ratio of 1:11.46, resulting in a total torque of approximately 333 Nm after the gearbox.

2.1.2 Steering actuator

An autonomous steering functionality is achieved through the use of a 220W brushless DC motor (2.2a) with a 3-stage planetary 1:43 gearbox from Maxon. The motor is equipped with an encoder that provides precise position information. Communication with the motor controller is established via the CAN bus. The motor's control loop regulates the position of the motor to match the request made by the autonomous system, which is the exact position of the steering shaft. A redundant measurement is taken using an absolute rotary encoder (2.2b). The motor operates at a voltage of approximately 37 V and a peak current of 20 A, resulting in a peak torque of 1.4 Nm and a peak speed of 5000 rpm. The angle of the front wheels can be determined with an accuracy of 0.01°.

(a) : 220W brushless DC motor[14] **(b) :** Absolute rotary encoder[15]

Figure 2.2: Motor assembly

2.1.3 Measurements

The SBG Systems inertial navigation system provides measurements of vehicle states, including position, velocity, and yaw rate, at a sample rate of 100 Hz. The product performs sensor fusion of accelerometers, gyroscopes, and GNSS data, resulting in 1 cm position accuracy, 0.01 m/s velocity accuracy and accuracy of 0.2° in heading.

Figure 2.3: INS Ellipse2-D[13]

2.2 IPG Carmaker

CarMaker by IPG Automotive [16] is a simulation software designed for the automotive industry. It specializes in the development and testing of vehicles, providing a comprehensive virtual environment for testing autonomous vehicles, ADAS, powertrain systems, and vehicle dynamics with high reliability and realism. The software is a multibody simulator that offers a user-friendly interface for vehicle parameterization, as the parameter count defining the car behavior is high. The user can define custom tires, aerofoil maps, suspension mechanics, electric and combustion powertrain, sensors, and more. The IPG Control app offers a signal viewing capability to analyze the simulation progress. Additionally, CarMaker provides a scenario designer that enables the user to define the track layout, maneuvers, road surfaces, elevation, traffic, and more. CarMaker is well known for its integration with Matlab Simulink, which makes the development of vehicle systems a lot easier.

2.2.1 FSE.12 CarMaker model

The team responsible for the development and maintenance of the formula models is eForce Prague Formula [17]. The FSE.12 vehicle model in IPG Carmaker was validated against a real car, therefore this thesis uses it as a verification model.

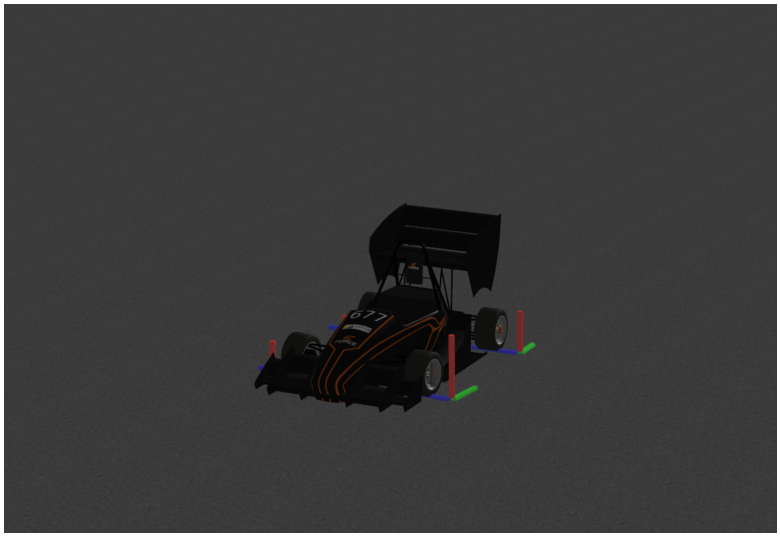

Figure 2.4: CarMaker eForce formula 3D visualisation

The model consists of three primary components: electric motors (wheel assembly), the monocoque, and the battery. The positions and masses of these components are defined, which determines most of the vehicle's moment of inertia, mass, and other properties. A suspension system is established, incorporating damper forces, spring behavior, and other suspension components. The aerodynamic behavior is defined using lookup tables that describe the

impact of aerofoils on vehicle motion. Parameters such as the coefficient of lift and drag are defined for various angles of incoming air. Parameters such as torque build-up time, moment of inertia, efficiency, and friction coefficients are specified for the powertrain setup. Tire characteristics are defined by a lookup table that varies based on normal forces and generates forces dependent on slip ratio or slip angle. The parameters, including rolling resistance factor, vertical/radial stiffness, and damping, are also defined. As the FSE.12 model does not include a motor for autonomous steering, it was approximated using the following transfer function:

$$G_{steer}(s) = \frac{75}{s + 75} \tag{2.1}$$

Chapter 3

Vehicle Dynamics Modeling

Modeling of four-wheeled vehicle dynamics is a control engineering topic described in various publications. The models can scale quickly and describe the car model in detail. For this thesis, described models were used, based on knowledge from [20]. If not said otherwise, all of the model speeds and angles are in the vehicle's center of gravity.

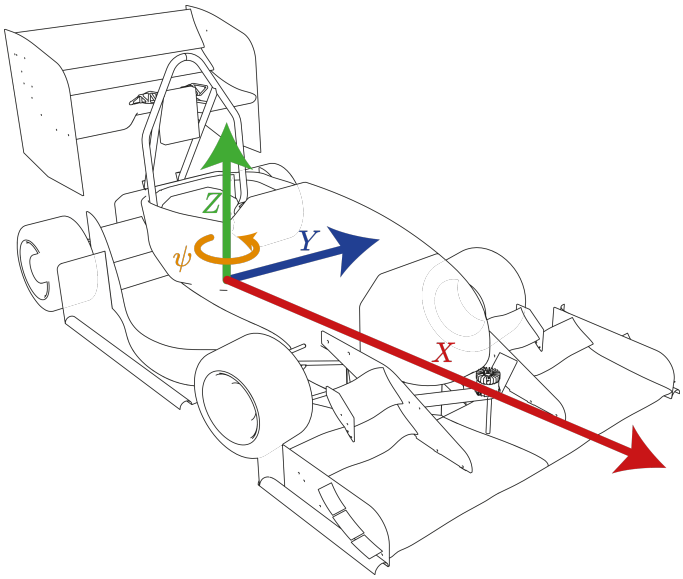

Figure 3.1: Vehicle body coordinate system

3.1 Coordinate systems

Both coordinate systems used in this thesis employ ISO8855. The vehicle coordinate system, also known as the body coordinate system, has the X-axis aligned with the direction of vehicle travel (longitudinal), while the Y-axis is perpendicular to the X-axis and points in the lateral direction. The Z-axis is perpendicular to both the X and Y axes and points upwards, completing the right-handed coordinate system. To improve the readability of the equations, the normal force F_z is considered positive, even if it acts in the opposite

direction of the Z-axis.
The local ground plane coordinate system is right-handed while fixed to the global plane. This thesis neglects the movement of the vehicle in the Z-axis, allowing only planar movement.

3.2 Non-linear Twin Track Model

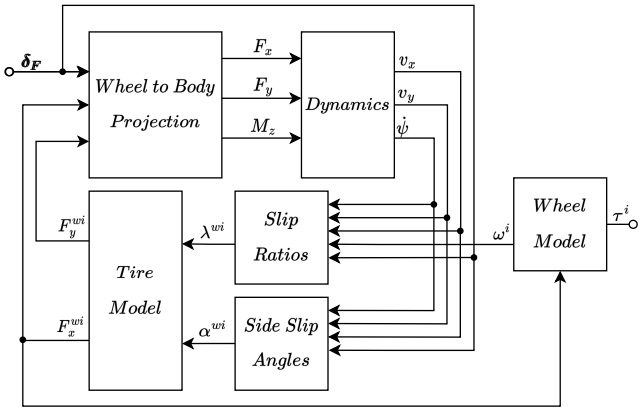

Figure 3.2: Architecture of non-linear twin-track model

The twin-track model offers advantages over the single-track model in its ability to describe more complex vehicle movements. The twin-track model can describe vehicle planar movement and generate angular motion from both the steering angle and torques on individual wheels. Its simplified architecture is shown in figure 3.2.

3.2.1 Wheel model

Assuming that all wheels have the same properties, the rotational acceleration can be described as

$$\dot{\omega}^{wi} = \frac{(\tau^{wi} - RF_x^{wi}(\lambda, F_z^{wi}, \mu^{wi}) - k_{r1}v_x^{wi} - k_{r2}F_z^{wi}(v_x^{wi}))}{J^{wi}} \tag{3.1}$$

where $\dot{\omega}$ $[rad/s^2]$ is the rotational acceleration of the wheel, J^{wi} is the moment of inertia of the wheel, and τ^{wi} is the moment applied to the wheel from the drivetrain. Braking torque is not considered, only braking via recuperation is available. The first negative component F_x^{wi} is the force transferred by the wheel on the road multiplied by the wheel radius R to obtain the reaction torque that acts on the drivetrain. The equation's last part represents the tire's rolling resistance, which is characterized by a second-order polynomial of v_x^{wi}, the wheel's velocity in its coordinate system (as shown in picture 3.3). The polynomial's coefficients are k_{r1} and k_{r2}. Note that the polynomial's second degree is not directly dependent on $(v_x^{wi})^2$, but on $F_z^{wi}(v_x^{wi})$, the normal force acting on the wheel. As stated in section 3.2.4, the impact of the aerofoil on the normal force increases quadratically with velocity.

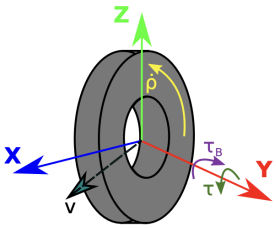

Figure 3.3: Wheel coordinate system [18]

3.2.2 Tire model

In vehicle dynamics, multiple tire models are used. Complex models include modeling with finite element methods, tire structure models, and brush models. In this thesis, the empiric model simplified Pacejka Magic Formula [19] is used.

$$F_x^{wi} = \mu^{wi} F_z^{wi} D_x \sin\left(C_x \arctan\left(B_x\lambda^{wi} - E_x(B_x\lambda^{wi} - \arctan\left(B_x\lambda^{wi}\right))\right)\right) \tag{3.2}$$

$$F_y^{wi} = \mu^{wi} F_z^{wi} D_y \sin\left(C_y \arctan\left(B_y\alpha^{wi} - E_y(B_y\alpha^{wi} - \arctan\left(B_y\alpha^{wi}\right))\right)\right) \tag{3.3}$$

Parameter $B_{x,y}$ is the stiffness factor, $C_{x,y}$ the cornering stiffness, $D_{x,y}$ the peak factor, and $E_{x,y}$ the curvature factor. The parameter μ^{wi} is used to model various road surfaces, where $\mu^{wi} = 1$ represents dry road and $\mu^{wi} = 0.6$ is for wet road.
The tire's lateral and longitudinal characteristics are a function of slip angle α and slip ratio λ^{wi}. The parameters of the lateral characteristics are calculated with α^{wi} expressed in radians or degrees. In this work, the coefficients are expressed in degrees. This equation represents the slip angle of the wheel:

$$\alpha^{wi} = -\arctan\left(\frac{v_y^{wi}}{v_x^{wi}}\right) \tag{3.4}$$

The slip ratios are then calculated as

$$\lambda^{wi} = \frac{\omega^{wi} R - v_x^{wi}}{\max(|\omega^{wi}|R, |v_x^{wi}|)} \qquad -1 \leq \lambda^{wi} \leq 1. \tag{3.5}$$

The longitudinal characteristics represented by the Pacejka magic formula for multiple normal forces F_z^{wi} can be seen on (3.4a). For the purpose of linearization, the tire characteristics are represented by the bilinear approximation (3.4b).
The expressed formulas are applicable only in isolated scenarios, where only longitudinal or lateral slip is taken into account. The friction ellipse describes the combined tire characteristics. This equation defines the constraint

$$\sqrt{\frac{(F_x^{wi})^2}{D_x^2} + \frac{(F_y^{wi})^2}{D_y^2}} \leq \mu^{wi} F_z^{wi}. \tag{3.6}$$

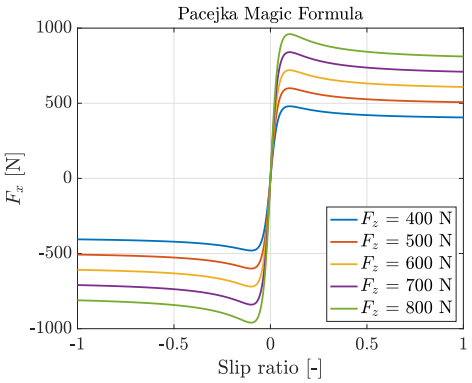

(a) : Pacejka Magic formula for multiple normal forces

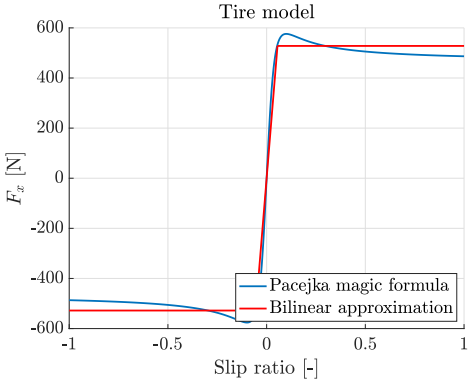

(b) : Bilinear approximation of Pacejka magic formula

Figure 3.4: Tire model

3.2.3 Wheel and body projections

Body to wheel projection

To calculate the tire effects on the vehicle dynamics described in 3.2.2, the wheel speeds $v_{x,y}^{wi}$ are obtained by these transformations

$$v_x^{wFL} = \left(v_x^v - \dot{\psi}\frac{d}{2}\right)\cos\delta_{FL} + (v_y^v + l_f\dot{\psi})\sin\delta_{FL} \tag{3.7}$$

$$v_x^{wFR} = \left(v_x^v + \dot{\psi}\frac{d}{2}\right)\cos\delta_{FR} + (v_y^v + l_f\dot{\psi})\sin\delta_{FR} \tag{3.8}$$

$$v_x^{wRL} = \left(v_x^v - \dot{\psi}\frac{d}{2}\right)\cos\delta_{RL} + (v_y^v - l_r\dot{\psi})\sin\delta_{RL} \tag{3.9}$$

$$v_x^{wRR} = \left(v_x^v + \dot{\psi}\frac{d}{2}\right)\cos\delta_{RR} + (v_y^v - l_r\dot{\psi})\sin\delta_{RR} \tag{3.10}$$

$$v_y^{wFL} = -\left(v_x^v - \dot{\psi}\frac{d}{2}\right)\sin\delta_{FL} + (v_y^v + l_f\dot{\psi})\cos\delta_{FL} \tag{3.11}$$

$$v_y^{wFR} = -\left(v_x^v + \dot{\psi}\frac{d}{2}\right)\sin\delta_{FR} + (v_y^v + l_f\dot{\psi})\cos\delta_{FR} \tag{3.12}$$

$$v_y^{wRL} = -\left(v_x^v - \dot{\psi}\frac{d}{2}\right)\sin\delta_{RL} + (v_y^v - l_r\dot{\psi})\cos\delta_{RL} \tag{3.13}$$

$$v_y^{wRR} = -\left(v_x^v + \dot{\psi}\frac{d}{2}\right)\sin\delta_{RR} + (v_y^v - l_r\dot{\psi})\cos\delta_{RR} \tag{3.14}$$

The distance from the center of gravity (CoG) to the front and rear axle of the car are represented by l_f and l_r, respectively. The track width of the car is denoted by d. Considering that the rear track is not steerable and the steering angle of the front wheels is the same, a substitution can be made

$\delta_{FL} \approx \delta_{FR} \approx \delta_F$, the equations are simplified to:

$$v_x^{wFL} = \left(v_x^v - \dot{\psi}\frac{d}{2}\right)\cos\delta_F + (v_y^v + l_f\dot{\psi})\sin\delta_F \tag{3.15}$$

$$v_x^{wFR} = \left(v_x^v + \dot{\psi}\frac{d}{2}\right)\cos\delta_F + (v_y^v + l_f\dot{\psi})\sin\delta_F \tag{3.16}$$

$$v_x^{wRL} = \left(v_x^v - \dot{\psi}\frac{d}{2}\right) \tag{3.17}$$

$$v_x^{wRR} = \left(v_x^v + \dot{\psi}\frac{d}{2}\right) \tag{3.18}$$

$$v_y^{wFL} = -\left(v_x^v - \dot{\psi}\frac{d}{2}\right)\sin\delta_F + (v_y^v + l_f\dot{\psi})\cos\delta_F \tag{3.19}$$

$$v_y^{wFR} = -\left(v_x^v + \dot{\psi}\frac{d}{2}\right)\sin\delta_F + (v_y^v + l_f\dot{\psi})\cos\delta_F \tag{3.20}$$

$$v_y^{wRL} = (v_y^v - l_r\dot{\psi}) \tag{3.21}$$

$$v_y^{wRR} = (v_y^v - l_r\dot{\psi}) \tag{3.22}$$

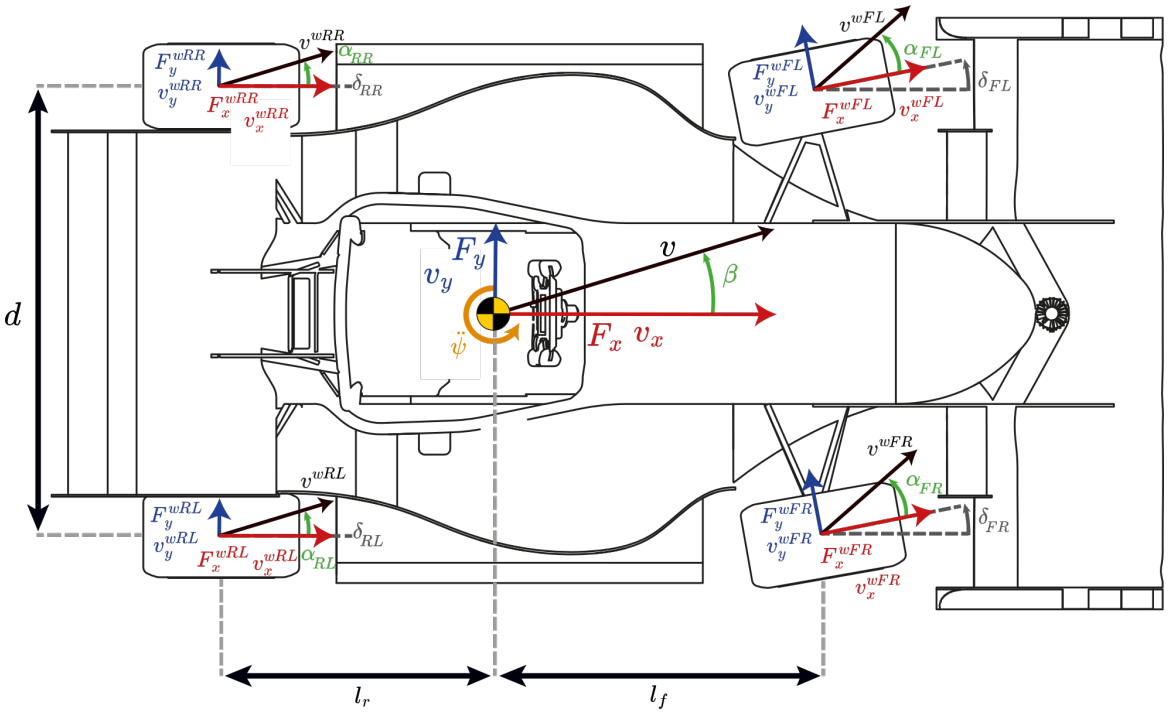

Figure 3.5: Top view of vehicle model

Wheel to body projection

Assuming the generated forces from 3.2.2, a form of transformation that will describe the forces applied on the vehicle body is needed. This set of

equations describes the force applied to the body.

$$F_x^{vFL} = F_x^{wFL}\cos\delta_{FL} - F_y^{wFL}\sin\delta_{FL} \tag{3.23}$$
$$F_x^{vFR} = F_x^{wFR}\cos\delta_{FR} - F_y^{wFR}\sin\delta_{FR} \tag{3.24}$$
$$F_x^{vRL} = F_x^{wRL}\cos\delta_{RL} - F_y^{wRL}\sin\delta_{RL} \tag{3.25}$$
$$F_x^{vRR} = F_x^{wRR}\cos\delta_{RR} - F_y^{wRR}\sin\delta_{RR} \tag{3.26}$$

$$F_y^{vFL} = F_x^{wFL}\sin\delta_{FL} + F_y^{wFL}\cos\delta_{FL} \tag{3.27}$$
$$F_y^{vFR} = F_x^{wFR}\sin\delta_{FR} + F_y^{wFR}\cos\delta_{FR} \tag{3.28}$$
$$F_y^{vRL} = F_x^{wRL}\sin\delta_{RL} + F_y^{wRL}\cos\delta_{RL} \tag{3.29}$$
$$F_y^{vRR} = F_x^{wRR}\sin\delta_{RR} + F_y^{wRR}\cos\delta_{RR} \tag{3.30}$$

Similarly, as in 3.2.3, the equation is further down simplified as

$$F_x^{vFL} = F_x^{wFL}\cos\delta_F - F_y^{wFL}\sin\delta_F \tag{3.31}$$
$$F_x^{vFR} = F_x^{wFR}\cos\delta_F - F_y^{wFR}\sin\delta_F \tag{3.32}$$
$$F_x^{vRL} = F_x^{wRL} \tag{3.33}$$
$$F_x^{vRR} = F_x^{wRR} \tag{3.34}$$

$$F_y^{vFL} = F_x^{wFL}\sin\delta_F + F_y^{wFL}\cos\delta_F \tag{3.35}$$
$$F_y^{vFR} = F_x^{wFR}\sin\delta_F + F_y^{wFR}\cos\delta_F \tag{3.36}$$
$$F_y^{vRL} = F_y^{wRL} \tag{3.37}$$
$$F_y^{vRR} = F_y^{wRR} \tag{3.38}$$

3.2.4 Aerodynamics

When examining how airfoil dynamics affect a vehicle's structure, simplified mathematical models are used. To calculate the force generated by the airfoil's lift in the vertical direction, the following equation is used:

$$F_{z_{aero}} = \frac{1}{2}\rho A_{ref} C_l v_x^2. \tag{3.39}$$

Similarly, the aerodynamic drag force is determined by the equation:

$$F_d = \frac{1}{2}\rho A_{ref} C_d v_x^2. \tag{3.40}$$

Here, A_{ref} represents the reference area of the airfoil, while ρ denotes the density of air. The coefficients of lift and drag are represented by C_l and C_d, respectively. To calculate the weight distribution on each wheel of the aerofoil's generated normal force, an equation is utilized:

$$F_{z_{aero}}^{wFL} = F_{z_{aero}}^{wFR} = (1 - CoP)\frac{d}{2}F_{z_{aero}}, \tag{3.41}$$
$$F_{z_{aero}}^{wRL} = F_{z_{aero}}^{wRR} = CoP\frac{d}{2}F_{z_{aero}}. \tag{3.42}$$

Where CoP is the center of dynamic pressure. It should be noted that this assumes the height of CoP is equivalent to the height of the center of gravity. Additionally, an assumption is made that the drag force only acts in the longitudinal direction of travel, neglecting the forces acting against the lateral motion and yaw rotation of the vehicle.

3.2.5 Tire normal forces distribution

As mentioned in the previous section, it must be noted that the weight distribution to all four wheels is not equal. The following equations calculated the weight distribution, assuming equal weight distribution in the lateral axis.

$$m^{wFL},\ m^{wFR} = \left(1 - \frac{l_f}{l}\right)\frac{m}{2} \tag{3.43}$$

$$m^{wRL},\ m^{wRR} = \left(1 - \frac{l_r}{l}\right)\frac{m}{2} \tag{3.44}$$

where l represents the total wheelbase of the car, while m represents its mass. The following equations were derived to consider the dynamic changes in normal forces on each tire while the car is accelerating.

$$F_{z_{dyn}}^{wFL} = -\frac{a_x m CoG_z}{2l} - \frac{a_y m CoG_z}{2d} \tag{3.45}$$

$$F_{z_{dyn}}^{wFR} = -\frac{a_x m CoG_z}{2l} + \frac{a_y m CoG_z}{2d} \tag{3.46}$$

$$F_{z_{dyn}}^{wRL} = \frac{a_x m CoG_z}{2l} - \frac{a_y m CoG_z}{2d} \tag{3.47}$$

$$F_{z_{dyn}}^{wRR} = \frac{a_x m CoG_z}{2l} + \frac{a_y m CoG_z}{2d} \tag{3.48}$$

The longitudinal and lateral accelerations are represented by a_x and a_y, respectively, while CoG_z denotes the height of the center of gravity. The calculation of the total normal force on each tire is as follows

$$F_z^{wi} = m^{wi} g + F_{z_{aero}}^{wi} + F_{z_{dyn}}^{wi}. \tag{3.49}$$

3.2.6 Vehicle dynamics

The final equations describing the planar motion of the vehicle are as follows.

$$a_x = \frac{F_x - F_d}{m} \qquad a_y = \frac{F_y}{m} \qquad \ddot{\psi} = \frac{M_z}{I_z} \tag{3.50}$$

Where F_x and F_y are forces acting on a car, M_z is the torque acting on a car, m is the car mass, and I_z is the car's moment of inertia. The F_x,F_y and M_z can be written as:

$$F_x = \sum_{i=1}^{4} F_x^{vi} \qquad F_y = \sum_{i=1}^{4} F_y^{vi} \tag{3.51}$$

$$M_z = \sum_{i=1}^{2} \begin{bmatrix} l_f \\ \frac{d}{2} \end{bmatrix} \times \begin{bmatrix} F_x^{vi} \\ F_y^{vi} \end{bmatrix} + \sum_{i=3}^{4} \begin{bmatrix} l_r \\ \frac{d}{2} \end{bmatrix} \times \begin{bmatrix} F_x^{vi} \\ F_y^{vi} \end{bmatrix}. \tag{3.52}$$

3.3 Control design models

3.3.1 Wheel speed controller design model

Referring to the equation 3.1, the v_x^{wi} can be replaced by $R\omega^{wi}$. Similarly, F_x^{wi} can be replaced by $F_z^{wi}\lambda^{wi}C_\lambda$ where C_λ is the coefficient of linear approximation of the Pacejka magic formula. Linearizing the slip ratio equation, an approximation can be introduced as $\Delta\lambda^{wi} = \frac{R\Delta\omega^{wi}}{v_x^{wi}}$. As the coefficient k_{r2} is small, the $k_{r2}F_z^{wi}(v_x^{wi})$ part of the equation is neglected. This results in the equation.

$$\Delta\dot{\omega}^{wi} = \frac{(\Delta\tau^{wi} - RF_z^{wi}\frac{R\Delta\omega^{wi}}{v_x^{wi}}C_\lambda - k_{r1}R\Delta\omega^{wi})}{J^{wi}} \tag{3.53}$$

3.3.2 Body velocity controller design model

Considering the vehicle moving in a straight line, equations 3.50 can be rewritten as

$$\Delta\dot{v}_x = \frac{\Delta F_x(\lambda, F_z, \mu) - \Delta F_d(v)}{m} \qquad \Delta a_y = 0 \qquad \Delta\ddot{\psi} = 0 \tag{3.54}$$

The equations can be further down written as

$$\Delta\dot{v}_x = \frac{\sum_{i=1}^{4} F_z^{wi}\Delta\lambda^{wi}C_\lambda - \rho A_{ref}C_d\Delta v_x}{m} \tag{3.55}$$

3.3.3 Yaw rate controller design model

Considering that the steering angles are 25 degrees at maximum, then approximations $\sin(\delta) \approx \delta$ and $\cos(\delta) \approx 1$ can be made. Thus, the equation for yaw acceleration can be rewritten as

$$\begin{aligned}\Delta\ddot{\psi}I_z =& \frac{d}{2}(-\Delta F_x^{wFL} + \Delta F_y^{wFL}\delta_F - \Delta F_x^{wRL} + \Delta F_x^{wFR} - \Delta F_y^{wFR}\delta_F + \Delta F_x^{wRR}) \\ &+ l_f(\Delta F_x^{wFL}\delta_F + \Delta F_y^{wFL} + \Delta F_x^{wFR}\delta_F + \Delta F_y^{wFR}) \\ &+ l_r(-\Delta F_y^{wRL} - \Delta F_y^{wRR}).\end{aligned} \tag{3.56}$$

The linear approximation of the wheel forces F_x^{wi} are used as in the 3.3.2. For the lateral characteristics, a linear approximation of the Pacejka magic formula with a C_α can be used. Thus resulting in the equation

$$\Delta F_y^{wi} = F_z^{wi}C_\alpha\Delta\alpha^{wi}. \tag{3.57}$$

Assuming that the slip angles are smaller than 30 degrees, the linear approximation of $\arctan(\frac{v_y}{v_x})$ is equal to $\frac{v_y}{v_x}$. With this, the equations 3.4 for

slip angles can be rewritten as

$$\alpha^{wFL} = \frac{\delta_F v_x^v - \delta_F \dot{\psi}\frac{d}{2} - v_y^v - l_f\dot{\psi}}{v_x^v - \dot{\psi}\frac{d}{2} + \delta_F v_y^v + \delta_F l_f \dot{\psi}}, \tag{3.58}$$

$$\alpha^{wFR} = \frac{\delta_F v_x^v + \delta_F \dot{\psi}\frac{d}{2} - v_y^v - l_f\dot{\psi}}{v_x^v + \dot{\psi}\frac{d}{2} + \delta_F v_y^v + \delta_F l_f \dot{\psi}}, \tag{3.59}$$

$$\alpha^{wRL} = \frac{-v_y^v + l_f\dot{\psi}}{v_x^v - \dot{\psi}\frac{d}{2}}, \tag{3.60}$$

$$\alpha^{wRR} = \frac{-v_y^v + l_f\dot{\psi}}{v_x^v + \dot{\psi}\frac{d}{2}}. \tag{3.61}$$

These equations can be further down simplified, assuming the $\delta_F\dot{\psi}\frac{d}{2} \ll 1$ and $\delta_F l_f\dot{\psi} \ll 1$. Another assumption is made that $v_x^v \gg \dot{\psi}$ and $v_x^v \gg \delta_F v_y^v$.

$$\Delta\alpha^{wFL} = \frac{\delta_F v_x^v - v_y^v - l_f\Delta\dot{\psi}}{v_x^v} \tag{3.62}$$

$$\Delta\alpha^{wFR} = \frac{\delta_F v_x^v - v_y^v - l_f\Delta\dot{\psi}}{v_x^v} \tag{3.63}$$

$$\Delta\alpha^{wRL} = \frac{-v_y^v + l_r\Delta\dot{\psi}}{v_x^v} \tag{3.64}$$

$$\Delta\alpha^{wRR} = \frac{-v_y^v + l_r\Delta\dot{\psi}}{v_x^v} \tag{3.65}$$

These equations describe the linear approximation of slip angles.

3.3.4 Kinematic Model

The kinematic model of a four-wheel vehicle constrains itself only on the front and rear axle of a car and thus does not use the width of the car. It also does not consider wheel slips. Car moves as described in the following equations.

$$\dot{\psi} = \frac{v\tan\delta_f\cos\beta}{l}, \tag{3.66}$$

$$v_x = v\cos(\beta+\psi), \tag{3.67}$$

$$v_y = v\sin(\beta+\psi), \tag{3.68}$$

where β is defined as

$$\beta = \arctan\left(\frac{l_r\tan\delta_f}{l}\right). \tag{3.69}$$

The kinematic model serves as a reference model for low-level controls. Therefore, the car controls itself to match the behavior of the kinematic model.

3.4 Model verification

3.4.1 Powertrain

Given the observation that the torque setpoint is not instantly achieved, a transfer function was derived based on the step response of the verification model. Experiments were conducted using various speeds and step sizes.

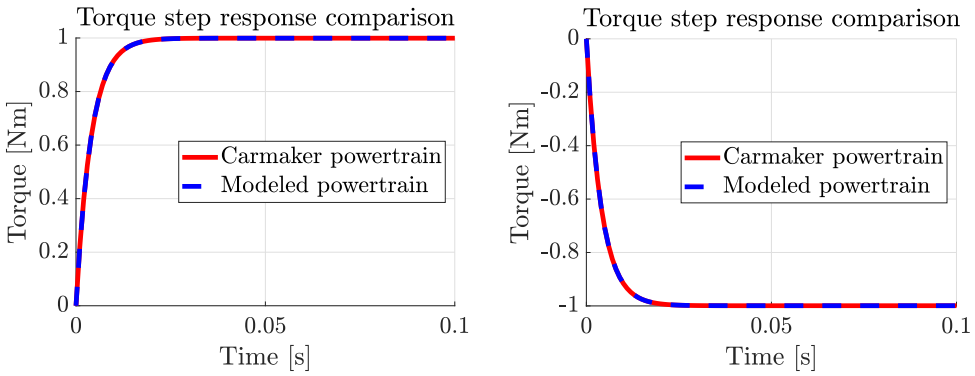

(a) : Positive torque step response

(b) : Negative torque step response

Figure 3.6: Electric powertrain dynamics

Figure 3.6 shows the results for two step sizes, 1 and -1. The transfer function $G_\tau(s)$ for the powertrain dynamics is represented by the following equation:

$$G_\tau(s) = \frac{248}{s + 248} \tag{3.70}$$

3.4.2 Drivetrain

Three experiments were conducted to evaluate the performance of the twin-track model's drivetrain and ensure its alignment with the verification model.

Each experiment began with a non-zero initial wheel speed. In all tests, the initial wheel speed was set to 4.83 [rad/s], matching the car speed of 1 m/s. The results of these tests are illustrated in figure 3.7, showcasing the system's response to torque steps of 0.5 Nm, 1 Nm, and 2 Nm. For clarity, only the behavior of the front left wheel is shown, as the remaining wheels exhibit similar behavior.

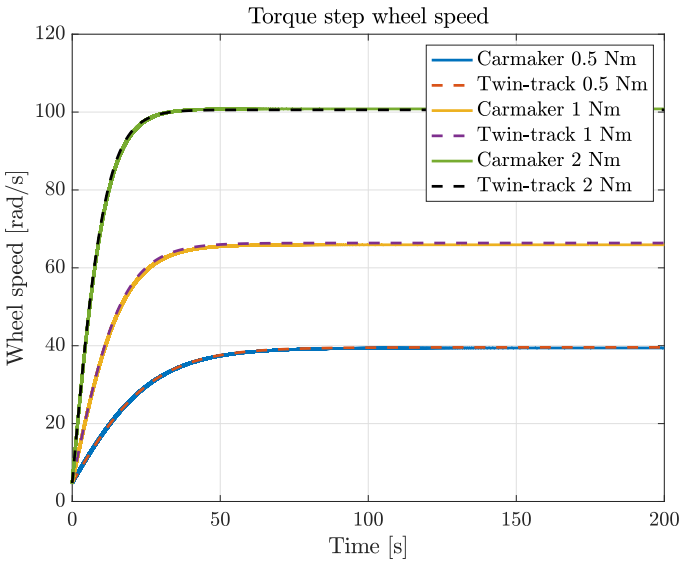

Figure 3.7: Wheel speed torque step response

3.4.3 Vehicle body

Similar experiments were conducted to validate the vehicle body behavior. The first experiment validates the model's behavior after applying 1 and 2 Nm of torque to the powertrain. In both cases, the vehicle's initial velocity is 1 m/s. The results can be observed in the figure 3.8 below. To validate

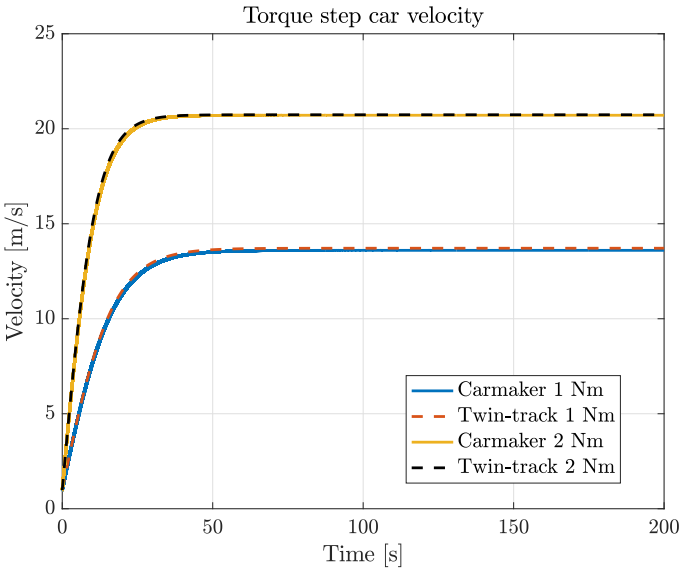

Figure 3.8: Vehicle speed torque step response

the yaw and lateral motion of the vehicle, a constant torque of 0.5 Nm was applied to all wheels, resulting in a longitudinal velocity of ≈ 8.28 m/s. After reaching a steady-state velocity, a sine wave with an amplitude of 25° and a

period of 2 seconds was applied to the vehicle's steering angle. The figure 3.9 below describe the behavior of the vehicle in this experiment.

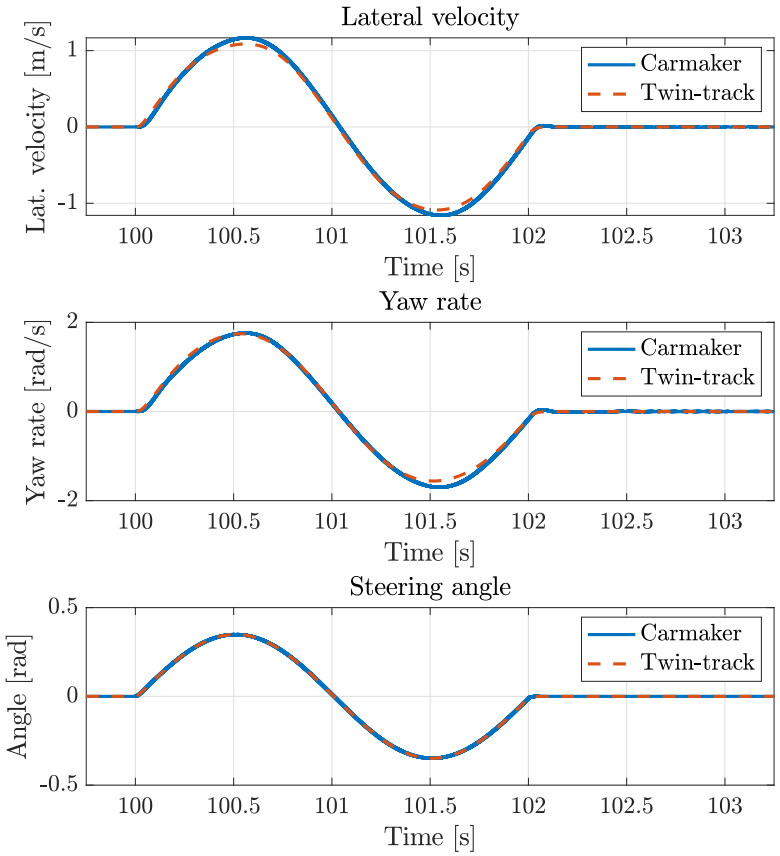

Figure 3.9: Vehicle body motion validation

3.4.4 Model parameters

The parameters of the twin-track model are shown in the following tables. Where the table 3.1 describes the general parameters of the vehicle.

Parameter	Value	Unit
m	201.2	kg
I_z	101.068	kg·m^2
l	1.53	m
l_f	0.7	m
l_r	0.823	m
d	1.2	m
CoG_z	0.042	m
g	9.81	m·s^{-2}
J^w	0.15	kg·m^2
R	0.207	m
k_{r1}	0.1	-
k_{r2}	0.025	-

Table 3.1: Table of vehicle parameters

The table 3.2 shows the parameters of the vehicle airfoil.

Parameter	Value	Unit
C_l	2.83	-
C_d	0.98	-
A_{ref}	1.51	m^2
ρ	1.205	kg·m^{-3}
CoP	0.7	-

Table 3.2: Table of aerofoil parameters

Lastly, the table 3.3 shows the twin-track Pacejka magic formula parameters.

Parameter	Value
B_x	20
C_x	1.4
D_x	1.2
E_x	-0.1
B_y	0.204
C_y	1.45
D_y	1.55
E_y	-0.3

Table 3.3: Table of Pacejka magic formula parameters

Chapter 4

Path-tracking algorithms

The figure 4.1 shows a cascade control system with two main controllers: the heading controller C_ψ is tuned to control the deviation from the reference heading ψ_{ref}, while $C_\perp$ controls the perpendicular deviation $e_\perp$ from the reference path $\boldsymbol{R}$. Additionally, a variable ψ_{LA} denotes the reference heading at a distance of d_{LA} along the reference path. The shadow vehicle block computes all the states required for the control systems. It takes in the car's position, reference, and lookahead distance as inputs. This architecture offers a significant advantage in that the C_ψ can be tuned independently only on the e_ψ. Once this is done, the other parts of the control system can be introduced. All controller designs are based on knowledge from [21] where the state space

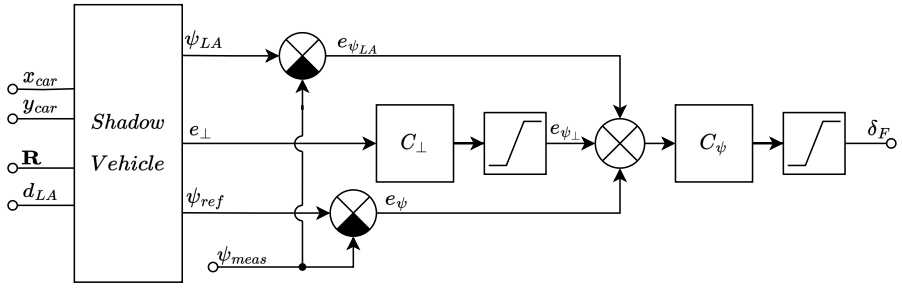

Figure 4.1: Path-tracking architecture

model 4.1 is derived.

$$\frac{d}{dt}\begin{bmatrix} e_\perp \\ \dot{e}_\perp \\ e_\psi \\ \dot{e}_\psi \end{bmatrix} = \begin{bmatrix} 0 \\ \frac{2C_{\alpha f}}{m} \\ 0 \\ \frac{2C_{\alpha f} l_f}{I_z} \end{bmatrix} \delta + \begin{bmatrix} 0 \\ -\frac{2C_{\alpha f} l_f - 2C_{\alpha r} l_r}{m v_x} - v_x \\ 0 \\ -\frac{2C_{\alpha f} l_f^2 + 2C_{\alpha r} l_r^2}{I_z v_x} \end{bmatrix} \dot{\psi}_{ref} + \begin{bmatrix} 0 \\ g \\ 0 \\ 0 \end{bmatrix} \sin(\phi)$$
$$+ \begin{bmatrix} 0 & 1 & 0 & 0 \\ 0 & -\frac{2C_{\alpha f} + 2C_{\alpha r}}{m v_x} & \frac{2C_{\alpha f} + 2C_{\alpha r}}{m} & \frac{-C_{\alpha f} l_f + C_{\alpha r} l_r}{m v_x} \\ 0 & 0 & 0 & 1 \\ 0 & -\frac{2C_{\alpha f} l_f - 2C_{\alpha r} l_r}{I_z v_x} & \frac{2C_{\alpha f} l_f - 2C_{\alpha r} l_r}{I_z} & -\frac{2C_{\alpha f} l_f^2 + 2C_{\alpha r} l_r^2}{I_z v_x} \end{bmatrix} \begin{bmatrix} e_\perp \\ \dot{e}_\perp \\ e_\psi \\ \dot{e}_\psi \end{bmatrix} \tag{4.1}$$

In the state space model, ϕ represents the bank angle, and g represents the gravitational acceleration of Earth.

Since the linear approximation coefficients $C_{\alpha f}$ and $C_{\alpha r}$ are equal and parameterized by the normal force F_z, the vehicle has only steerable front wheels, the bank angle and weight distribution are not considered. The resulting state space model is represented as follows:

$$\frac{d}{dt}\begin{bmatrix} e_\perp \\ \dot{e}_\perp \\ e_\psi \\ \dot{e}_\psi \end{bmatrix} = \begin{bmatrix} 0 \\ \frac{C_{\alpha F_z}}{2m} \\ 0 \\ \frac{C_{\alpha F_z} l_f}{2I_z} \end{bmatrix} \delta_F + \begin{bmatrix} 0 \\ -\frac{C_\alpha F_z l_f - C_\alpha F_z l_r}{2mv_x} - v_x \\ 0 \\ -\frac{C_\alpha F_z l_f^2 + C_\alpha F_z l_r^2}{2I_z v_x} \end{bmatrix} \dot{\psi}_{ref}$$
$$+ \begin{bmatrix} 0 & 1 & 0 & 0 \\ 0 & -\frac{C_\alpha F_z}{mv_x} & \frac{C_\alpha F_z}{m} & \frac{-C_\alpha F_z l_f + C_\alpha F_z l_r}{2mv_x} \\ 0 & 0 & 0 & 1 \\ 0 & -\frac{C_\alpha F_z l_f + C_\alpha F_z l_r}{2I_z v_x} & \frac{C_\alpha F_z l_f - C_\alpha F_z l_r}{2I_z} & -\frac{C_\alpha F_z l_f^2 + C_\alpha F_z l_r^2}{2I_z v_x} \end{bmatrix} \begin{bmatrix} e_\perp \\ \dot{e}_\perp \\ e_\psi \\ \dot{e}_\psi \end{bmatrix}. \quad (4.2)$$

4.1 Error calculation

The algorithm for calculating errors takes the reference matrix as input, which contains information about the entire reference path. The reference matrix consists of 2D plane coordinates $x,\ y$ that describe the path, as well as two additional pieces of information about the road surface's friction coefficients. The first coefficient denotes the friction coefficient μ_{refL} for the left side of the road, and the second coefficient μ_{refR} denotes the friction coefficient for the right side of the road.
The algorithm first calculates the nearest point index $\boldsymbol{p}_n$, on the reference path $\boldsymbol{R}$ from the car's position $\boldsymbol{p}_{car}$. The situation is shown in figure 4.2

$$\boldsymbol{p}_n = \underset{\boldsymbol{p}_i \in \boldsymbol{R}}{\operatorname{argmin}} \, ||\boldsymbol{p}_i - \boldsymbol{p}_{car}|| \quad (4.3)$$

Then, it creates a spline using the points surrounding the closest point on the reference path. This results in a smoother reference than the original. Finally, it calculates the closest point $\boldsymbol{p}_\perp$ on that spline from the car's position, using the 4.3 equation. The point $\boldsymbol{p}_\perp$ approximates the orthogonal projection of the car's position on the reference path, and it is often referred to as a shadow vehicle. This approximation becomes more accurate as the spline evaluation becomes finer. Therefore, the error is negligible.

At the point $\boldsymbol{p}_\perp$, a tangent estimation is computed because evaluating the tangent directly on the spline is computationally inefficient. The tangent vector $\boldsymbol{p}_t$ is estimated using the preceding and succeeding points. Using the tangent vector $\boldsymbol{p}_t$ and *atan2* function, the reference heading ψ_{ref} is calculated. As the *atan2* [22] function is defined on closed interval $[-\pi, \pi]$, the edge cases have to be handled.

The car's signed lateral deviation from the path is referred to as the cross-track error $e_\perp$. The distance is calculated between the car's position and the tangent vector $\boldsymbol{p}_t$ to determine the cross-track error. The following equation

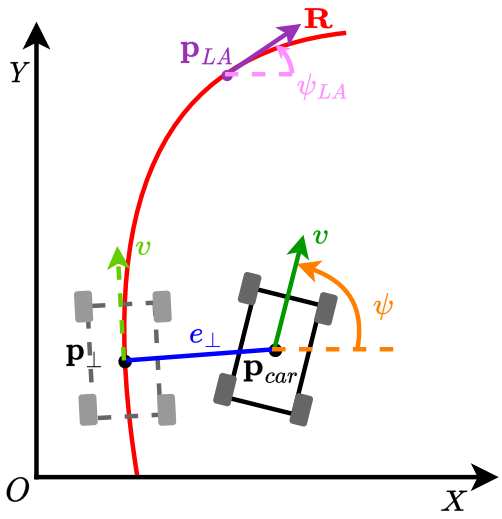

Figure 4.2: Shadow vehicle illustration

is used to determine the sign $s_{e\perp}$ of the cross-track error.

$$s_{e\perp} = sign\left(\boldsymbol{p}_t \times (\boldsymbol{p}_c - \boldsymbol{p}_\perp)\right) \tag{4.4}$$

Finally, the algorithm needs to locate the lookahead heading. It starts at the point $\boldsymbol{p}_\perp$ and iterates through the following points, summing the distance between them. If the sum exceeds the lookahead distance d_{LA}, the iteration stops. A spline is created using surrounding points, similar to when calculating the $\boldsymbol{p}_\perp$, and the iteration continues on the spline, summing the distances between the spline points. If the sum of the distances in the next step is greater than the lookahead distance d_{LA}, the heading is evaluated at that point, resulting in a lookahead heading ψ_{LA}.

4.2 Controllers

4.2.1 Heading controller

As previously stated, the heading controller is tuned separately. The e_ψ represents the heading deviation from the referential path. The controller outputs the command for the steering actuator in terms of the front wheel angle δ_F. The transfer function 4.5 can be derived using the state space model 4.2.

$$\frac{\Delta\psi_{ref}}{\Delta\delta_F} = \frac{l_f v_x}{\left(l_f^2 + l_r^2\right) s} \tag{4.5}$$

The controller was designed to have a maximum overshoot of 20% and a settling time of $T_s < 1\ s$. The heading controller design is presented in figure 4.3.

Note that the transfer function 4.5 depends on the vehicle velocity v_x. The controller was designed for a working velocity of 10 m/s. Therefore, it needs

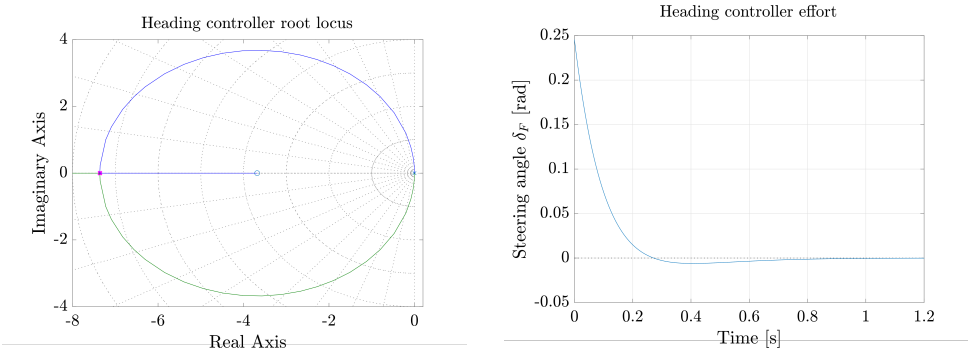

(a) : Yaw controller root locus

(b) : Yaw controller effort

Figure 4.3: Yaw controller design

to be verified for multiple velocities. Figure 4.4 illustrates this behavior. As shown, the controller meets the design requirements, except for velocities lower than 5 m/s. However, this behavior is neglected because, as mentioned earlier, the driving speeds in all disciplines are greater than 5 m/s.

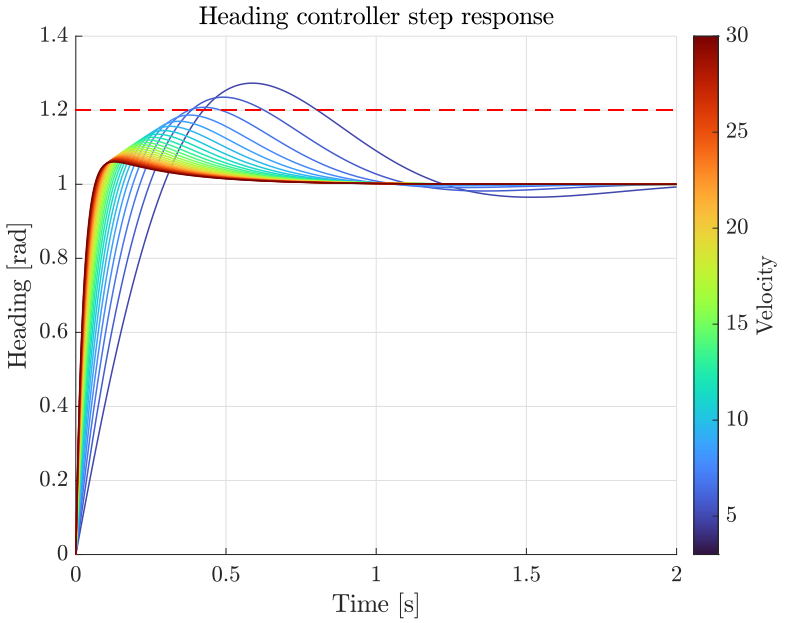

Figure 4.4: Heading controller step response for multiple velocities

As both the cross-track and heading controllers are reactive, the controller introduces a predictive component with the lookahead heading $e_{\psi LA}$. The distance that the vehicle looks ahead is determined by its current velocity. As the velocity increases, so does the lookahead distance, as described by the following equation.

$$d_{LA} = v_x k_{LA} \tag{4.6}$$

Where k_{LA} represents the dependency of lookahead distance on velocity. The k_{LA} parameter is used to tune the controller. A higher k_{LA} value results in

more predictive actions taken by the controller.
Finally, the gain parameter k_{eLA} is introduced to adjust the impact of the lookahead heading on the final heading action.

4.2.2 Cross-track controller

Utilizing the state space model from 4.2, a transfer function can be deducted where the $e_\perp$ is the input to the controller and e_ψ the output.

$$\frac{\Delta e_\perp}{\Delta e_\psi} = \frac{\frac{C_\alpha F_z(-l_f+l_r)}{2mv_x}s + \frac{C_\alpha F_z}{m}}{\frac{C_\alpha F_z}{mv_x}s} \tag{4.7}$$

This transfer function can be further down simplified to:

$$\frac{\Delta e_\perp}{\Delta e_\psi} = \frac{(-l_f + l_r)\,s + 2v_x}{2s}. \tag{4.8}$$

The controller is designed to have an overshoot of less than 20% and a transient response time of less than 3 seconds. The root locus 4.5 represents the system with the controller designed for a working speed of $10m/s$. Similar

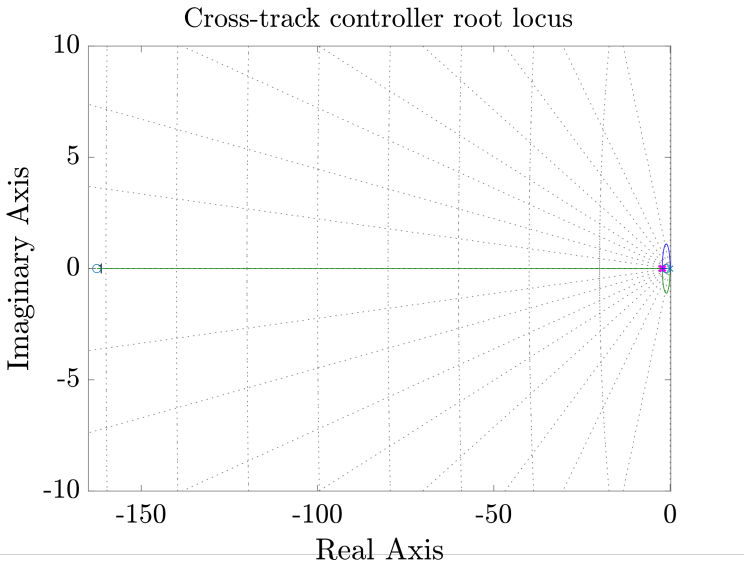

Figure 4.5: Cross-track controller root locus

to the heading controller, the transfer function on which the controller design is based is velocity dependent, so it must be verified for multiple velocities. The system behavior with the designed controller for different speeds is shown in figure 4.6.

An observation is made that the designed controller does not meet the design requirements for velocities less than 5 m/s. As discussed earlier, the path-tracking algorithms do not have to meet the design requirements for velocities less than 5 m/s.

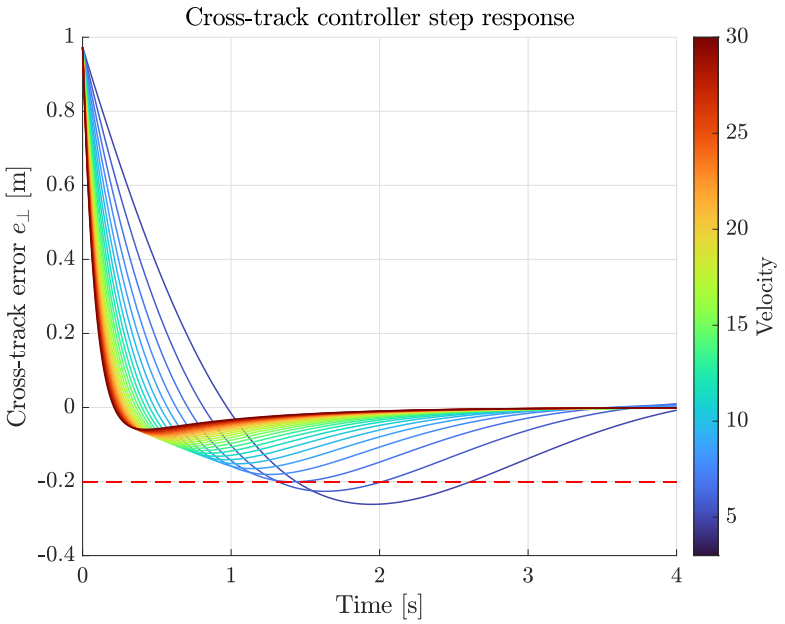

Figure 4.6: Cross-track controller step response for multiple speeds

To address the issue of cross-track controller aggressiveness at higher velocities, the resulting action is scaled using the following equation:

$$e_{\psi\perp} = \frac{e_{o\psi\perp}}{k_{soft} + v_x}. \tag{4.9}$$

The original action generated by the cross-track controller is labeled as $e_{o\psi\perp}$, while the new corrected action is $e_{\psi\perp}$. To ensure less aggressive behavior for low velocities, a tunable parameter called k_{soft} is used.

Chapter 5

Vehicle dynamics control

A cascade architecture was chosen for the vehicle dynamics control architecture due to its easy tunability. The system architecture 5.1 starts with a kinematic model, which serves as the reference model. The inputs are the vehicle velocity v_x and the steering angle δ_F. The kinematic model then generates the reference yaw rate $\dot{\psi}_{ref}$. Following the reference kinematic model, two parallel controllers are introduced: the velocity controller, which controls the longitudinal velocity of the vehicle body, and the yaw rate controller, which controls the yaw rate of the vehicle body. The velocity controller outputs the slip ratio λ, while the yaw rate controller outputs the difference in slip ratio, $\Delta\lambda$, between the left and right sides of the vehicle. The slip ratios from each wheel are distributed respectively by the λ distribution box, which combines the outputs of the two controllers. The wheel speeds are then calculated from the slip ratios. Finally, the wheel speed controller adjusts the rotational speed of each wheel, producing torque as output.

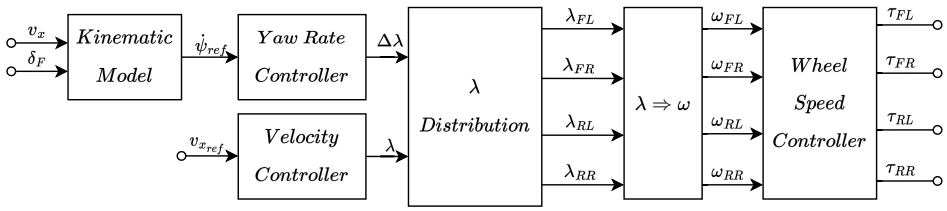

Figure 5.1: Low-level control system architecture

5.1 Wheel speed controller

After applying the Laplace transform to the linear model of the wheel referred to in 3.3.1, the following equation is obtained.

$$\omega^{wi}(s)s = \frac{(\tau^{wi}(s) - RF_z^{wi}\frac{R\omega^{wi}(s)}{v_x^{wi}}C_\lambda - k_d R\omega^{wi}(s))}{J^{wi}} \tag{5.1}$$

Considering the ω^{wi} as output and τ^{wi} as the input, the transfer function has this form

$$\frac{\omega^{wi}(s)}{\tau^{wi}(s)} = \frac{1}{J^{wi}s + \frac{R^2 F_z^{wi} C_\lambda}{v_x^{wi}} + k_d R} \tag{5.2}$$

It should be noted that the transfer function 5.2 assumes that the car body is stationary while the wheel spins, thus generating a slip. It is important to observe that the system behavior is strongly affected by the operating speed at which the transfer function is calculated. For speeds lower than 5 m/s, the pole position changes rapidly, as shown in figure 5.2.

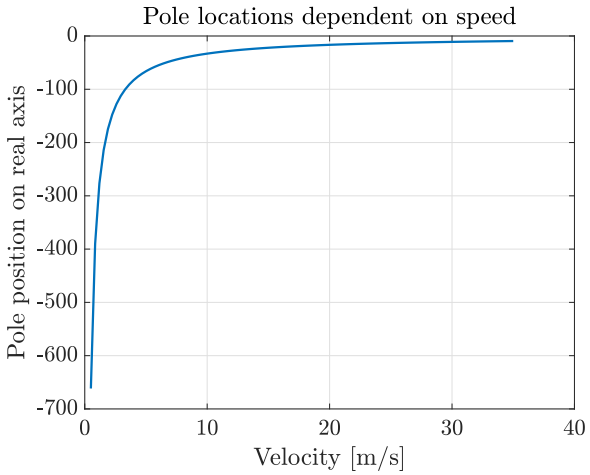

Figure 5.2: Pole position based on the wheel speed v_x^w

To ensure system controllability, controllers for multiple speeds must be designed. The root locus design method was chosen, and controllers were designed to have a settling time of less than 0.01 seconds. For instance, the root locus for controller design for a speed of 2 m/s is depicted in the figure 5.3.

The controllers for speeds 1, 2, 3, 4, 5, 7, 10, and 20 m/s were designed similarly. However, it is necessary to design more controllers within the range of 1 m/s to 10 m/s due to the rapid changes in their P and I parameters. As a result, the I and P parameters of the PI controller are functions of speed, as shown in the picture 5.4. The best-fitting proportional gain function have a shape of $P(v) = \frac{a_P v^2 + b_P v + c_P}{d_P v^2 + e_P v + f_P}$, while the integral gain function is represented by $I(v) = \frac{a_I v + b_I}{c_I v + d_I}$.

The controller scheme shown in figure 5.5 deviates from the conventional PI controller scheme. τ_0 is the initial condition, which is parametrized by velocity, and ω_{ref} is the reference rotational wheel speed, with ω_{meas} representing its actual rotational speed. Finally, an anti-windup method clamping is used to eliminate any unwanted integral behavior. If the controller's output is saturated, the integration is paused.

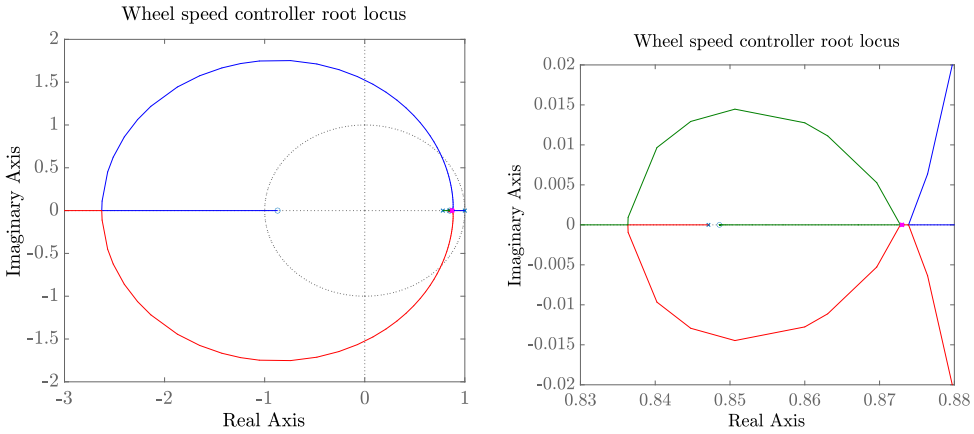

(a) : Full root locus **(b) :** Zoomed root locus

Figure 5.3: Root locus of system with controller for 2 m/s

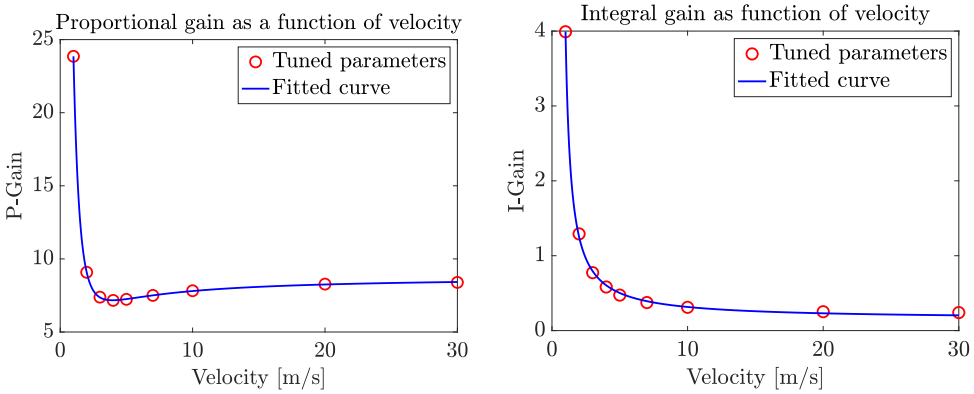

(a) : Proportional gain function **(b) :** Integral gain function

Figure 5.4: Fitted curves for proportional and integral gains

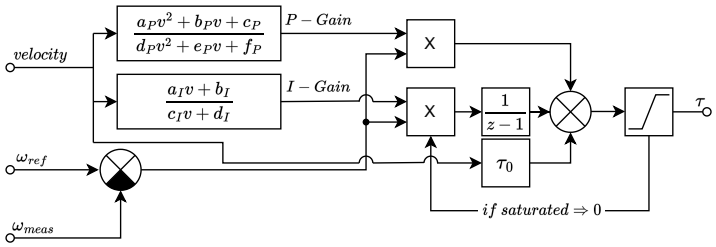

Figure 5.5: Wheel speed controller scheme

5.2 Slip ratio controller

Considering the equation for slip ratio

$$\lambda = \frac{\omega R - v_x^w}{\max(|\omega| R, |v_x^w|)} \tag{5.3}$$

where lambda is the function of wheel speed v_x^w and rotational wheel speed ω. It is possible to modify this function to obtain a formula for the rotational wheel ω, which depends on the slip ratio and wheel speed. Since the slip ratio function is non-linear, there will be four equations describing the rotational wheel speed as a function of slip ratio and wheel speed.

$$\omega(v_x^w, \lambda) = \begin{cases} \frac{v_x^w}{R}\frac{1}{1-\lambda_{ref}} & v_x^w > 0,\ \lambda_{ref} \geq 0 \\ \frac{v_x^w}{R}(1+\lambda_{ref}) & v_x^w > 0,\ \lambda_{ref} \leq 0 \\ \frac{v_x^w}{R}(1-\lambda_{ref}) & v_x^w < 0,\ \lambda_{ref} \geq 0 \\ \frac{v_x^w}{R}\frac{1}{1+\lambda_{ref}} & v_x^w < 0,\ \lambda_{ref} \leq 0 \end{cases} \tag{5.4}$$

In these equations, λ_{ref} represents the reference slip ratio requested by the velocity and yaw rate controllers. The slip ratio reference is saturated to permit a maximum of 10% slip, resulting in nearly optimal usage of the slip curve.

5.3 Slip ratio distribution

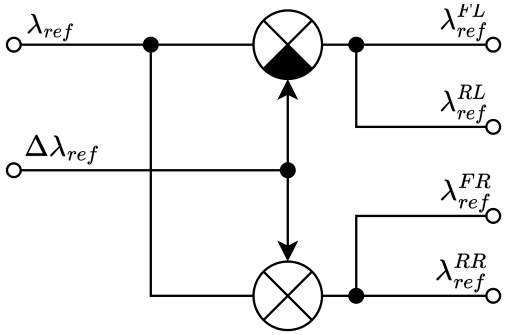

Figure 5.6: Slip ratio distribution scheme

The slip ratio distribution follows a straightforward architecture in which the same slip ratio required by the velocity controller is set to all four wheels while simultaneously lowering the slip ratio on one side and raising it on the other. This ensures priority to the yaw controller in addition to the velocity.

5.4 Velocity controller

Applying Laplace transform on equation 3.55 results in

$$v_x(s)s = \frac{F_z\lambda(s)C_\lambda - F_d}{m}. \tag{5.5}$$

Given that λ is an action variable, the transfer function can be expressed as follows:

$$\frac{\Delta v_x(s)}{\Delta \lambda(s)} = \frac{C_\lambda \left(g + \frac{F_{z_{aero}}}{m}\right)}{s + \frac{\rho A_{ref} C_d v_x}{m}}. \tag{5.6}$$

To achieve rapid changes in velocity, the controller was designed to operate mostly in saturation while maintaining an overshoot of less than 20%. The controller's saturation, which is based on the longitudinal characteristic of the Pacejka magic formula, is set at a 10% slip ratio. The design of the system at velocity 10 m/s with the velocity controller can be seen in figure 5.7.

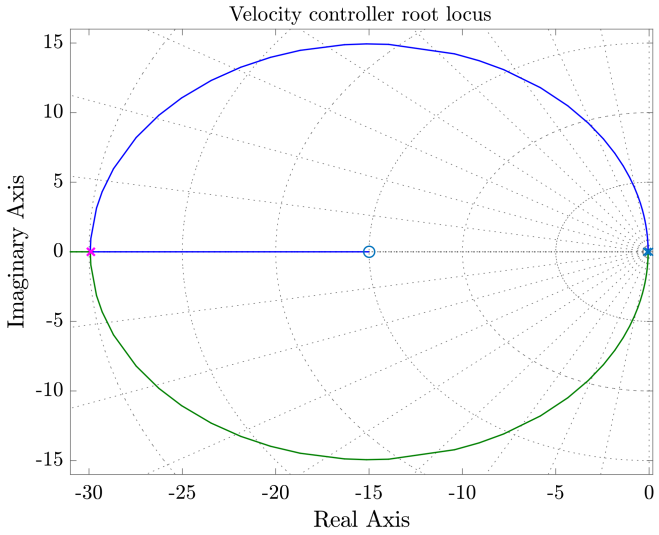

Figure 5.7: Velocity controller design

It can be observed that the velocity controller depends on the current vehicle velocity. It is necessary to verify the controller's performance at different velocities. The system's behavior with the controller at various velocities is shown in the figure 5.8, while the controller effort at various velocities can be seen in 5.9.

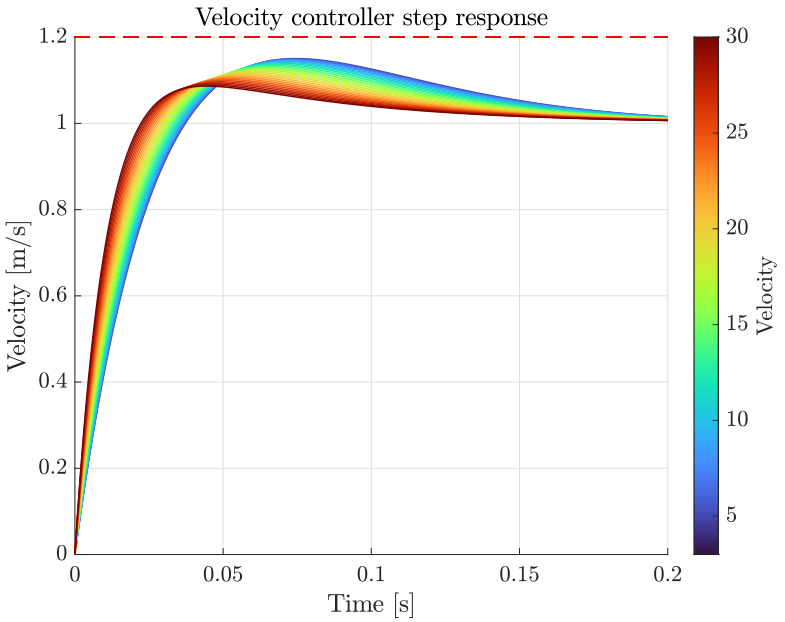

Figure 5.8: Velocity controller step response for various velocites

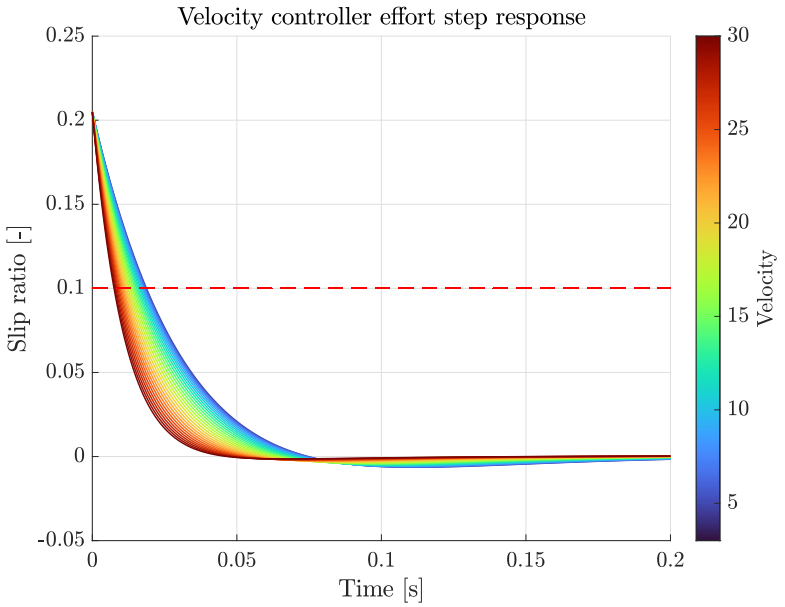

Figure 5.9: Velocity controller effort step response for various velocites

5.5 Yaw rate controller

The yaw rate controller receives the desired yaw rate from the reference kinematic model and produces the slip distribution $\Delta\lambda_{ref}$ between the left and right sides of the vehicle. The slip distribution can be rewritten as:

$$\Delta\lambda_{ref} = -\lambda^{L}_{ref} = \lambda^{R}_{ref}. \tag{5.7}$$

To differentiate between $\Delta\lambda_{ref}$ and the divination form of λ used in transfer function equations, a substitution of $\Delta\lambda_{ref} = \lambda_{\dot{\psi}}$ is employed. Using the equation 3.56, a transfer function 5.8 can be derived that describes the relationship between the slip ratio and the yaw motion of the vehicle.

$$\frac{\Delta\dot{\psi}}{\Delta\lambda_{\dot{\psi}}} = \frac{\frac{C_\lambda F_z d}{2I_z}}{s + \frac{C_\alpha F_z \left(l_f^2 + l_r^2\right)}{2I_z v_x}} \tag{5.8}$$

The yaw controller uses a PI controller designed for a working point velocity of 10 m/s. The response of the controller is restricted by the performance of

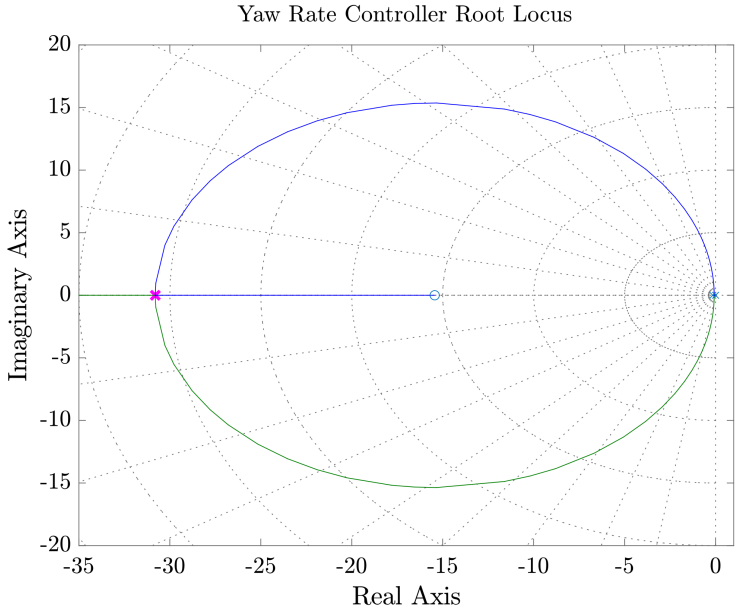

Figure 5.10: Root locus of yaw rate controller

the wheel speed controller. Hence, it was designed to have a response time faster than 0.3 seconds and an overshoot of up to 20%. Similar to the velocity controller, the yaw rate controller is also velocity-dependent. Therefore, it needs to be verified for multiple velocities. This controller behavior and effort are shown in figures 5.11,5.12, respectively.
It can be observed that the response of the controller does not appear to be significantly affected by changes in velocity.

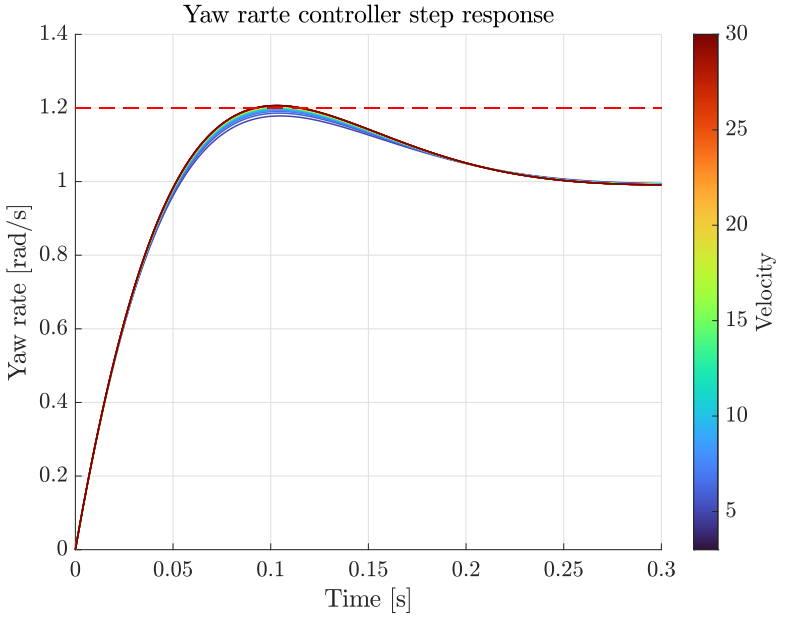

Figure 5.11: Yaw rate controller step response for various velocites

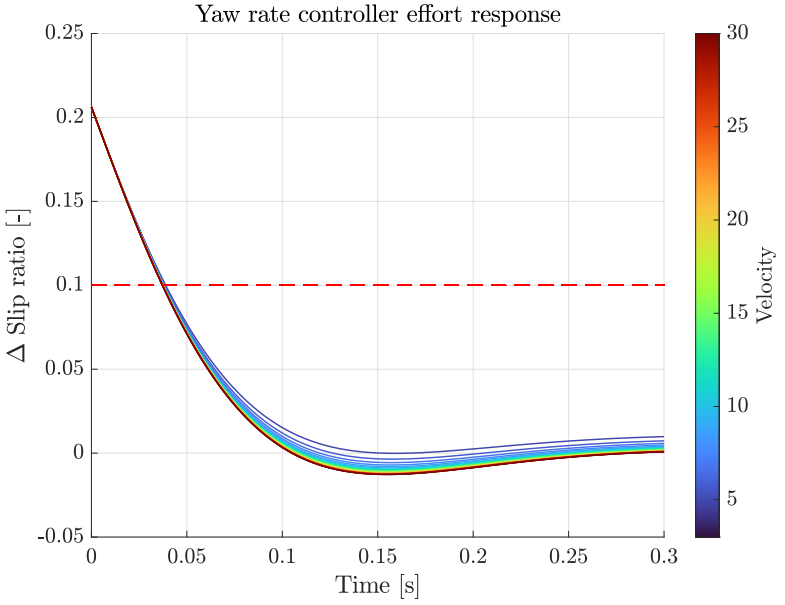

Figure 5.12: Yaw rate controller step response for various velocites

Chapter 6

Experiments

6.1 Vehicle dynamics control

6.1.1 Wheel speed controller

The wheel speed controller underwent several experiments to test its performance in the linear area of the tire characteristics, excluding the nonlinear tire behavior on the controller action. The tests involve a 1% change in the desired wheel speed, which results in a maximum slip ratio of 1%. This ensures that the tire characteristics remain linear. Following experiments were conducted to observe the effect of changing controller parameters with the velocity: step response at 5 m/s, 15 m/s, and 30 m/s. As observed in the

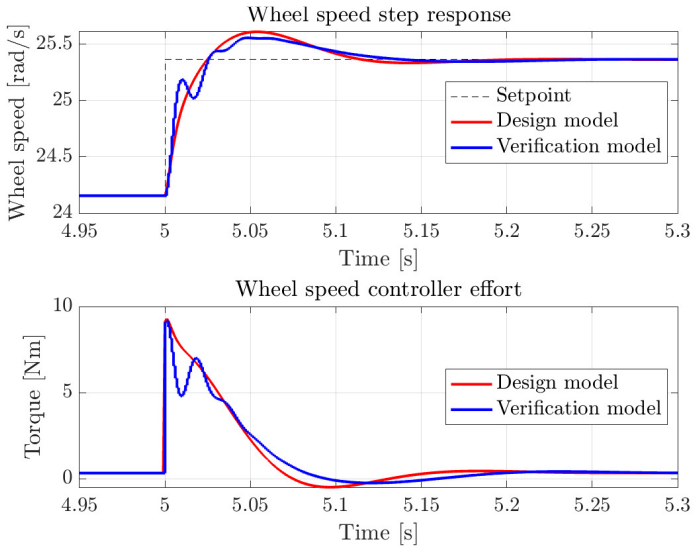

Figure 6.1: Wheel speed step response at 5 m/s

verification model, there are signs of unmodeled dynamics compared to the design model, resulting in small oscillations in the wheel speed. Although this behavior is not ideal, the oscillations do not cause the controller to lower the applied torque to less than zero. Frequent transitions between positive

and negative torques are not beneficial for the drivetrain, as there is some play in the transmission, and frequent changes can result in increased play, thus lowering the lifespan.

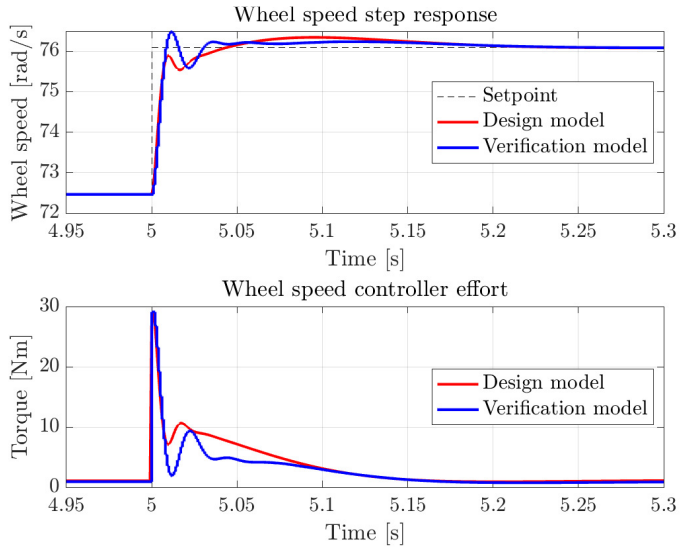

Figure 6.2: Wheel speed step response at 15 m/s

As shown in figure 6.3, the verification and design models differ in their response.

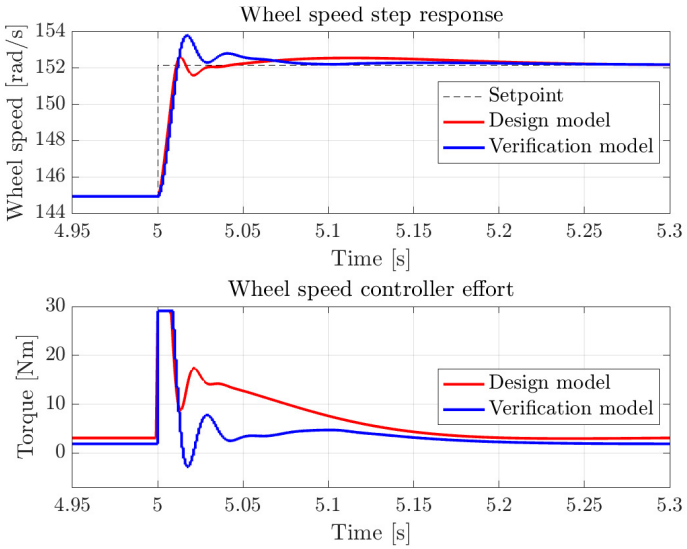

Figure 6.3: Wheel speed step response at 30 m/s

The verification model reaches the desired speed in the same amount of time, although with a slight overshoot. This difference may be attributed to unmodeled high-velocity dynamics, such as the changing diameter of the tire,

which results in varying forces. In contrast to the first experiment, it can be observed that both the design model and the verification model oscillate. This behavior is likely caused by the controller's overly aggressive actions. In conclusion, the verification model with the wheel speed controller satisfies the defined requirement of a maximum settling time of 0.1 seconds. However, it introduces oscillations due to overly aggressive controller and unmodeled dynamics.

6.1.2 Slip ratio controller

To validate the slip ratio controller, an experiment was conducted. A slip ratio of 5% was requested, followed by a request for -5% slip ratio after 1 second.

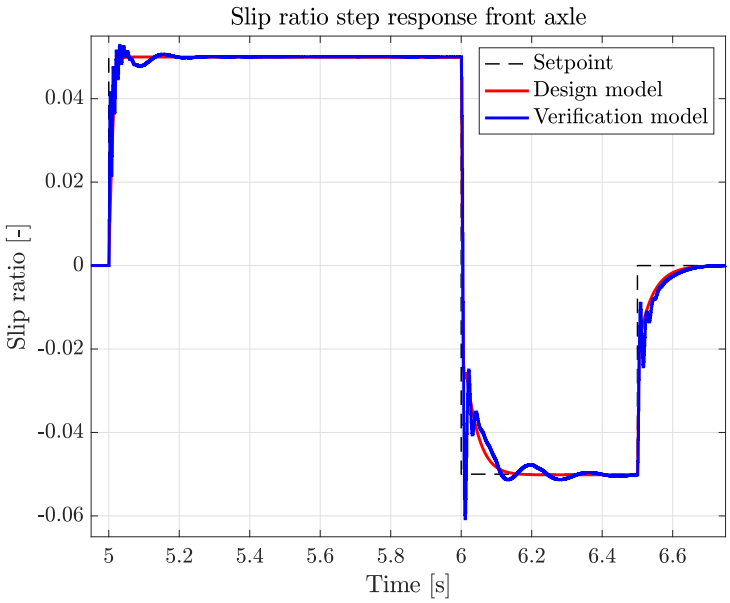

Figure 6.4: Front left slip ratio controller response

The test unveils the non-ideal wheel's speed controller, which introduces small oscillations at the rise of the slip ratio setpoint. As the weight distribution changes when accelerating, the slip differs on the front and rear axle as shown in the figures 6.4 and 6.5

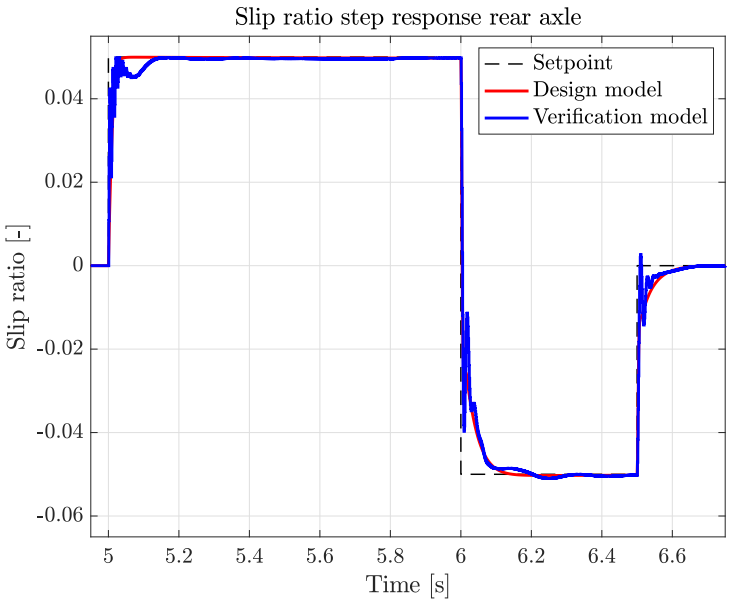

Figure 6.5: Rear left slip ratio controller response

Additionally, to verify the controller's ability to withstand rapid changes in road surface conditions, a test called μ jump was conducted. The test consists of changing the road surface friction coefficient on all four wheels, effectively lowering it to friction coefficient of $\mu = 0.6$. Such an experiment is shown in figure 6.6.

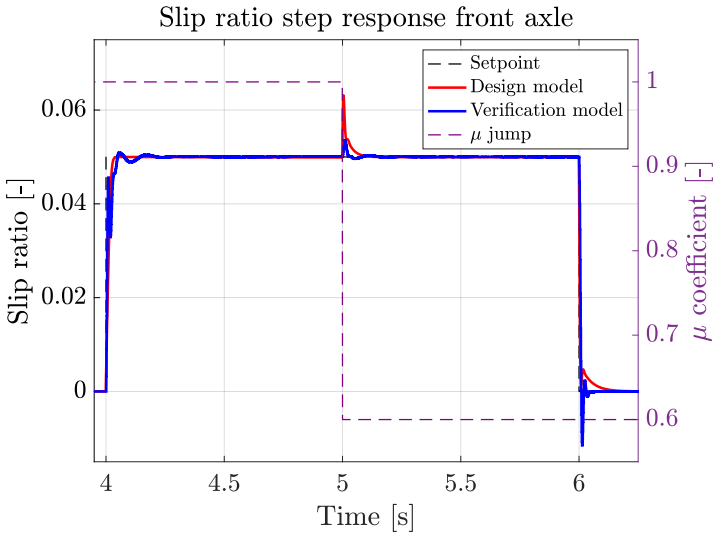

Figure 6.6: Slip ratio controller μ jump test

As can be observed, the slip ratio controller is able to withstand rapid changes in the road surface.

6.1.3 Velocity controller

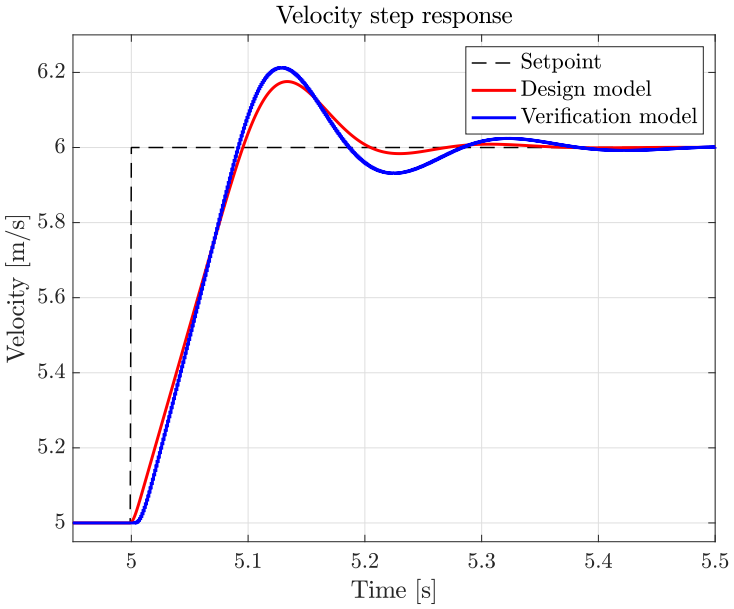

Figure 6.7: Velocity controller step response

The velocity controller nearly fulfills the design requirements, having an overshoot of less than 20%, as it reaches an overshoot of 21%. The slight deviation from the design model is most likely caused by the wheel's speed controller. The controller effort is shown in figure 6.8. To test the controller's

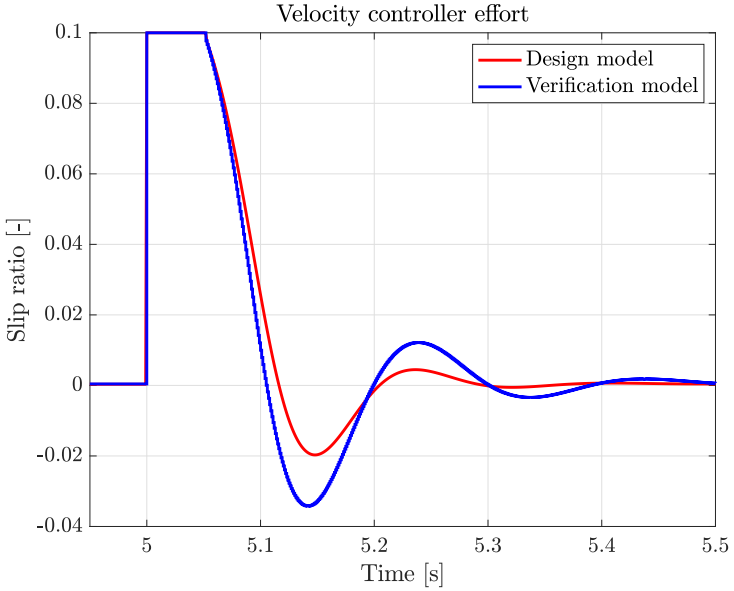

Figure 6.8: Velocity controller step response effort

ability to handle larger changes in velocity, an experiment was conducted where the speed was reduced from 10 m/s to 5 m/s. Additionally, the μ

jump was included in this experiment to demonstrate the behavior of the controller when the road surface changes. The figure 6.9 shows a change in

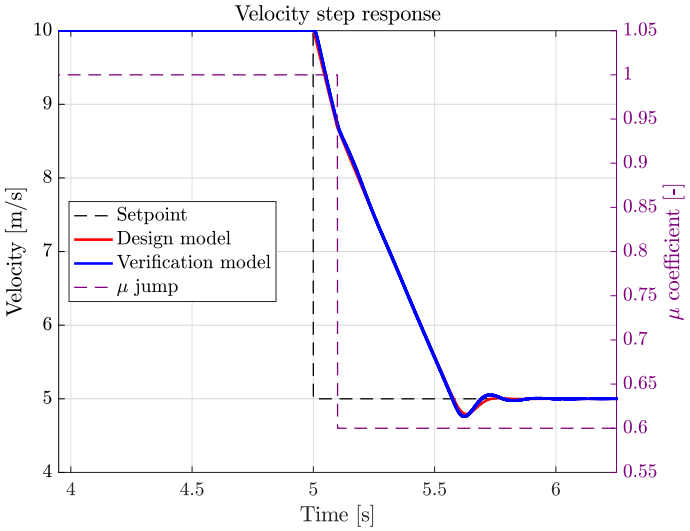

Figure 6.9: Velocity controller step response with μ jump

deceleration as the road surface changes. In this case, the controller responses for both the design and verification models are nearly identical. The figure 6.10 displays the controller effort, which indicates that the velocity controller is not affected by changes in the road surface. This is because it is controlled by the slip ratio controller.

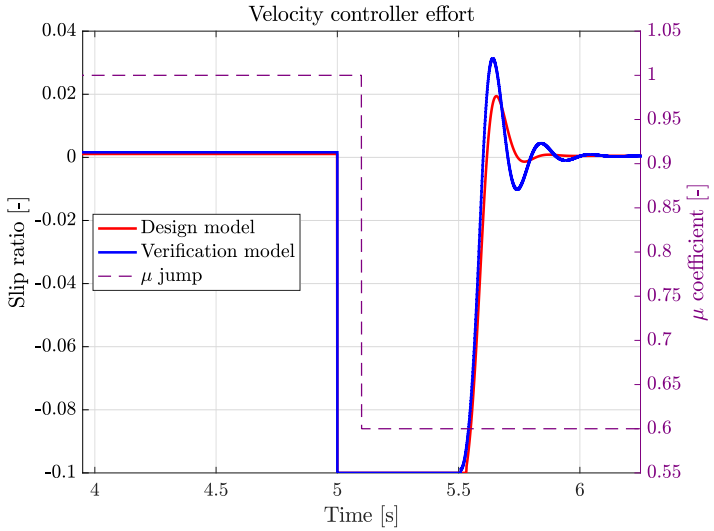

Figure 6.10: Velocity controller step response effort with μ jump

6.1.4 Yaw rate controller

To verify the behavior of the yaw rate controller, a sine wave of amplitude 10 degrees and a period of 0.5 seconds was applied to the vehicle's steering

angle at the vehicle's velocity of 10 m/s. The kinematic model generates the reference yaw rate. This maneuver is dynamic and suitable for verification purposes. The figure 6.11a demonstrates the added benefit of the yaw rate controller.

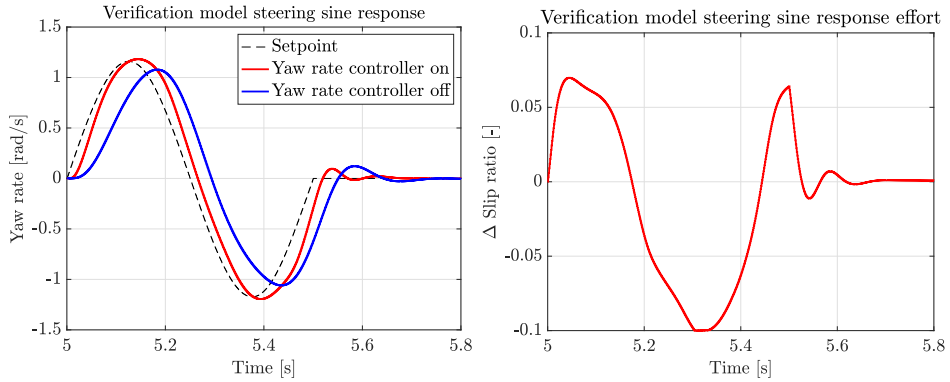

(a) : System response **(b) :** Controller effort

Figure 6.11: Verification model 10 degrees steering sine wave maneuver at 10 m/s

It has been observed that the vehicle's yaw motion aligns more closely with the setpoint generated by the kinematic model when the yaw rate controller is activated. Figure 6.12a shows similar behavior in the design model.

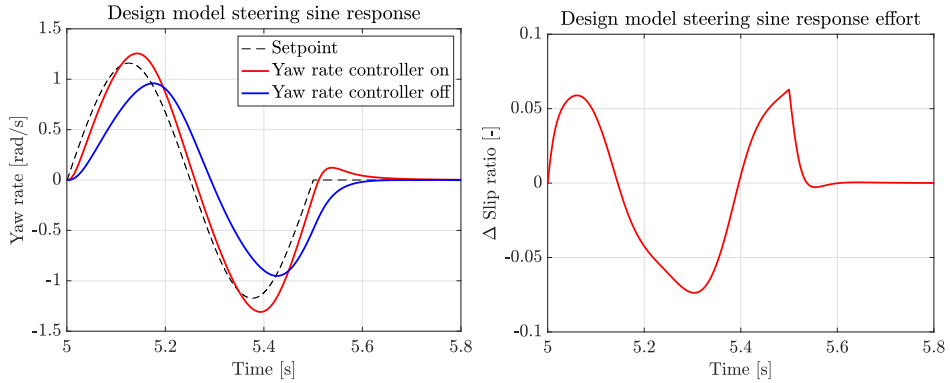

(a) : System response **(b) :** Controller effort

Figure 6.12: Design model 10 degrees steering sine wave maneuver at 10 m/s

As the yaw rate controller is suitable for multiple velocities, a similar test with an amplitude of 5 degrees at 25 m/s was conducted.
The figures 6.13a and 6.14a demonstrate that the significance of the yaw rate controller increases with the vehicle's velocity as the vehicle's yaw rate fails to reach the kinematic model behavior without it.

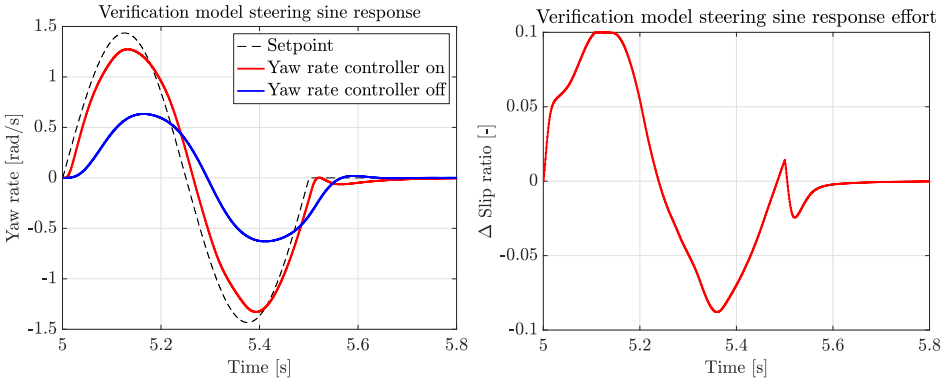

(a) : System response **(b) :** Controller effort

Figure 6.13: Verification model 5 degrees steering sine wave maneuver at 25 m/s

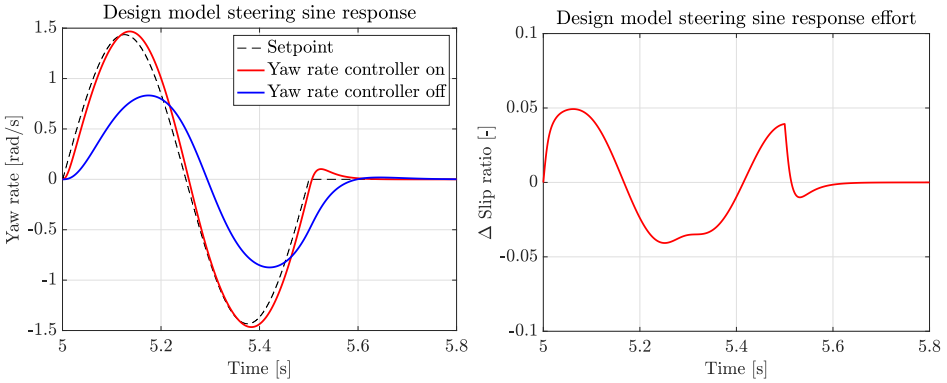

(a) : System response **(b) :** Controller effort

Figure 6.14: Design model 5 degrees steering sine wave maneuver at 25 m/s

However, as shown in figures 6.13b and 6.14b, the effort of the controllers varies between the verification and design models, revealing unmodeled dynamics in the design model. Since the system yaw rate response remains unchanged, this behavior can be neglected.
To demonstrate the controller's ability to withstand changes in the road surface, a step steer maneuver was conducted while having a μ split. The μ split lowers the friction coefficient for one side of the vehicle.
In this experiment, the vehicle's right side had a lower friction coefficient of $\mu = 0.6$. The velocity was 20 m/s, and the step size of the steering angle was 5 degrees.

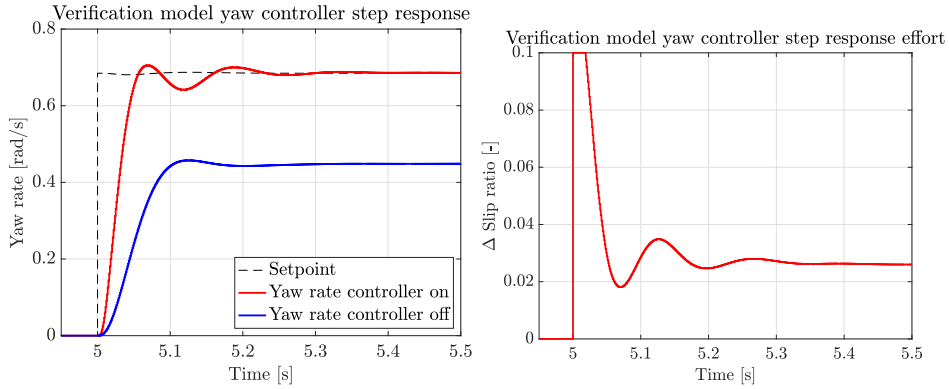

(a) : System response **(b) :** Controller effort

Figure 6.15: Verification model 5 degrees steering angle step response with 0.6 μ split

When the vehicle loses friction on the right wheels, it cannot achieve the necessary yaw rate itself. To address this, the yaw rate controller increases the slip ratio on the right side and decreases it on the left side to account for the varying road surfaces, as can be observed in figure 6.15b.
Finally, a ramp steer test was conducted to demonstrate the significance of the yaw rate controller during cornering. The test was performed at a velocity of 10 m/s with a ramp slope of 2 applied to the steering angle.
The figure 6.16 shows that when the yaw rate controller is active, the vehicle can achieve higher yaw rates while maintaining the same velocity. Additionally,

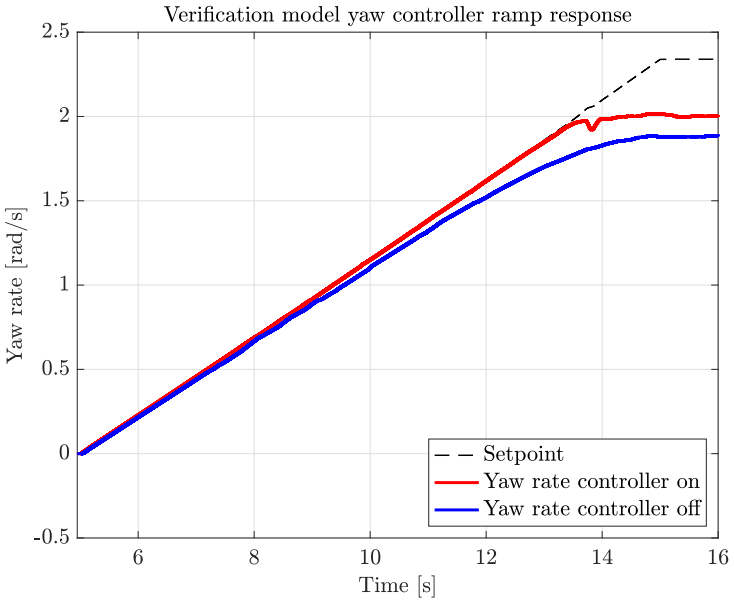

Figure 6.16: Verification model ramp steer response at 10 m/s

a similar test was conducted at a velocity of 20 m/s. The figure 6.17 displays the test results with and without the yaw controller activated, where the

statement from the previous experiment is confirmed. It is evident that when the yaw rate controller fails to reach the setpoint, the system introduces oscillations. This is due to the fact that the vehicle is skidding and the yaw rate controller is attempting to manage the vehicle's behavior. Since the yaw rate controller is not designed for this scenario, a different controller should be implemented to manage this situation.

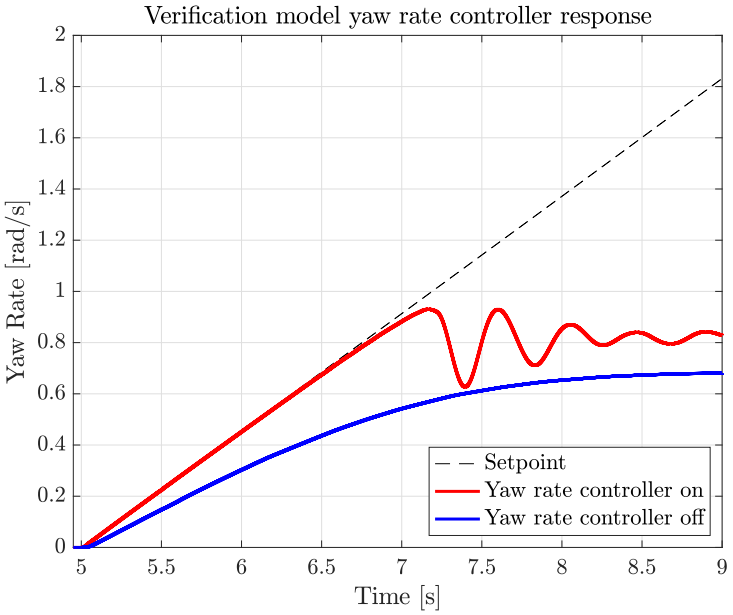

Figure 6.17: Verification model ramp steer response at 20 m/s

6.2 Path tracking

The first path-tracking experiment consists of U-turns with diameters of 10 and 20 meters, respectively. Another test is the S-turn, which effectively tests the ability to maintain steady-state cornering while changing direction mid-test. The S-turn diameter is designed to simulate the skidpad track and approximate the vehicle's behavior in that discipline. Finally, a straight path is used to test the ability to return to the track with initial conditions set to the maximum deviations observed in the competition.

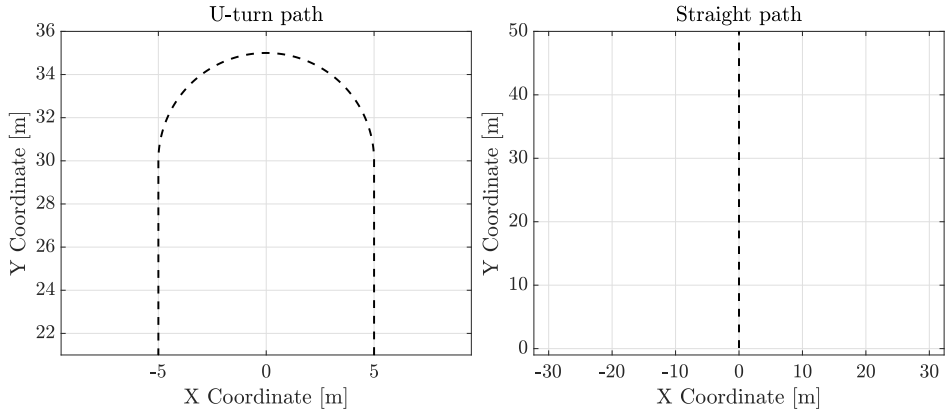

(a) : U-turn path **(b) :** Straight path

Figure 6.18: Path configurations

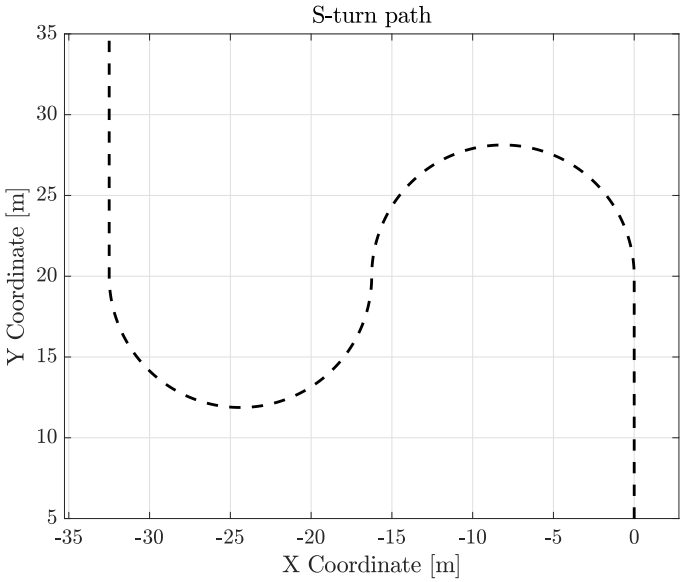

Figure 6.19: S-turn path

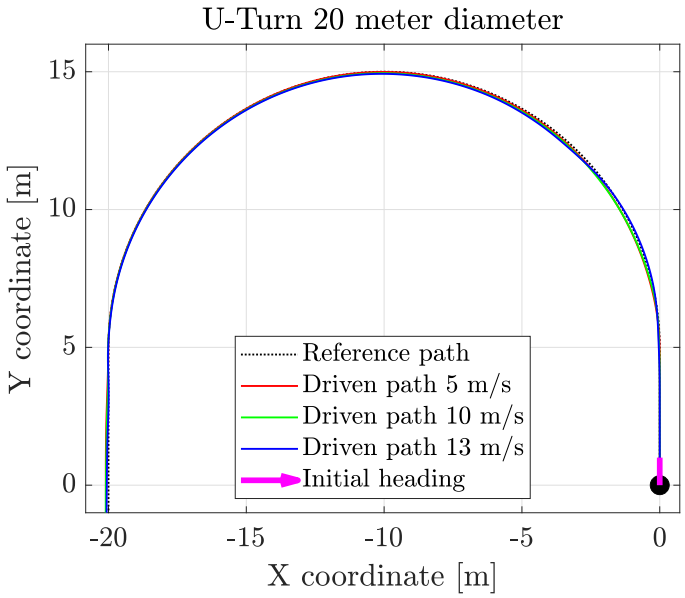

Figure 6.20: U-turn of 20 m diameter at velocities of 5, 10 and 13 m/s

6.2.1 U-Turn

Firstly, a larger diameter U-turn test was conducted for velocities of 5, 10, and 13 m/s.
Figure 6.21 demonstrates the path-tracking ability to match the reference heading. A small oscillation is observed at a velocity of 13 m/s, which might be caused by the fact that 13 m/s was the maximum feasible velocity for this maneuver.

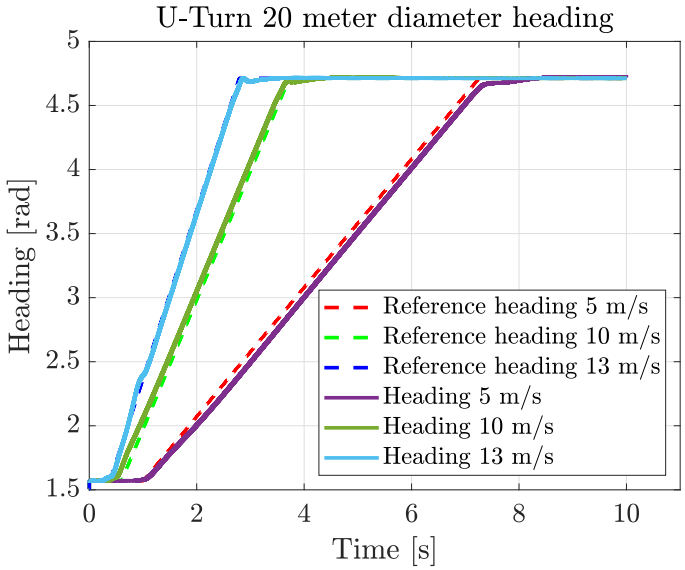

Figure 6.21: U-turn of 20 m diameter reference heading tracking

The fact that the vehicle is conducting the maneuver near maximum feasible

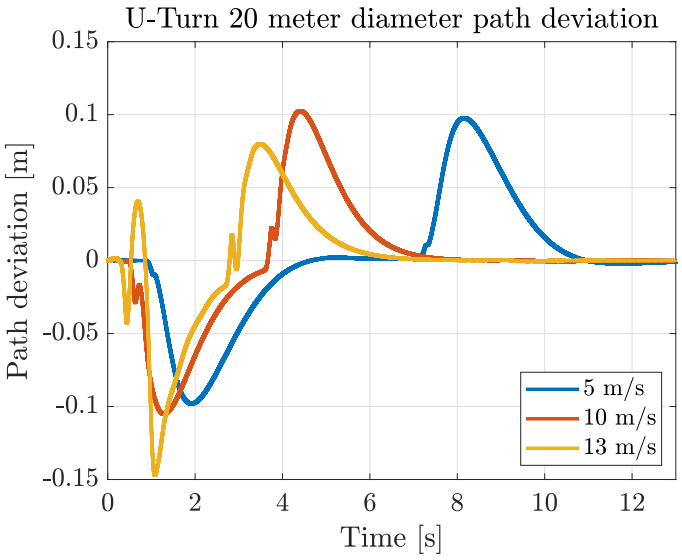

Figure 6.22: U-turn of 20 m diameter cross track error

velocity, is also evident in figure 6.22, where the cross-track error for a velocity of 13 m/s spikes to 0.15 meters. For the remaining velocities, the lateral deviation from the track does not exceed 0.1 meters. The peak in the cross-track error occurs when the vehicle enters or exits the circular path. The steering actions generated by the path-tracking are shown in figure 6.23.

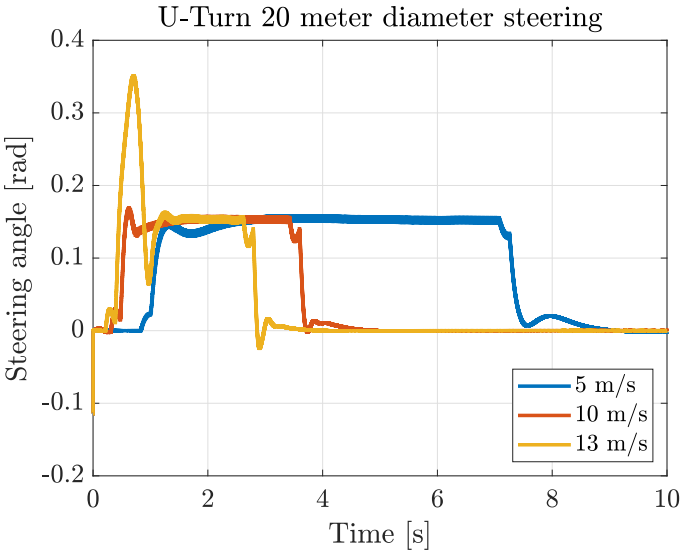

Figure 6.23: U-turn of 20 m diameter steering command

Figure 6.24 demonstrates the second 10-meter diameter U-turn experiment at a velocity of 7 m/s. It can be observed that the path-tracking does not accurately follow the reference path.
Furthermore, figure 6.25 illustrates that the cross-track error exceeded 0.15 meters during the turn, eventually settling to zero in the straightaway. The

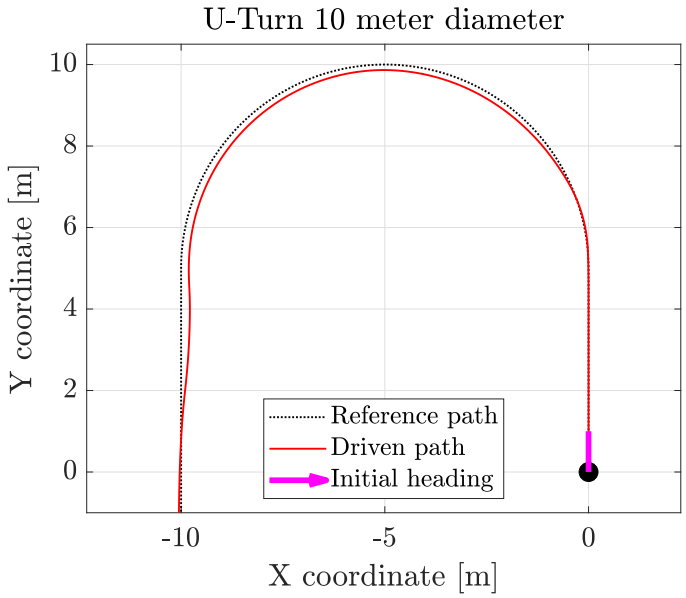

Figure 6.24: U-turn of 10 m diameter at a velocity of 7 m/s

test was conducted at various velocities, yielding similar results. For sharp turns like this one, the controller with the calculated parameters is not adequate, and the settings should be changed for such paths.

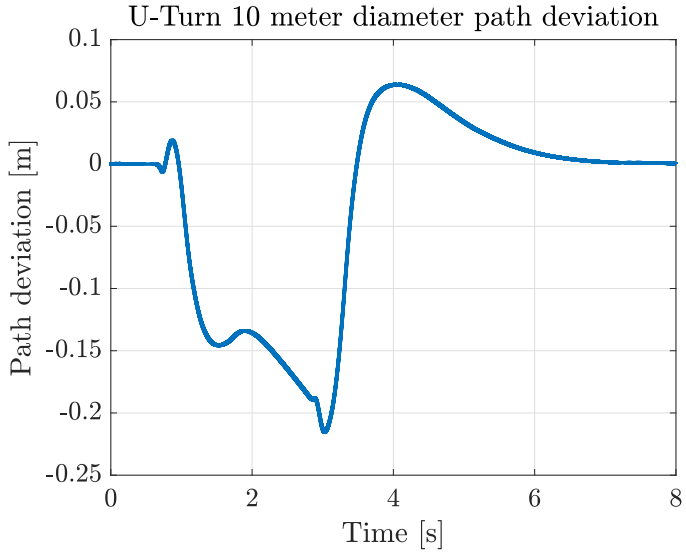

Figure 6.25: U-turn of 10 m diameter cross track error

6.2.2 Straight

Two tests were conducted to demonstrate the path-tracking ability to drive on the track when not positioned precisely in the start area. The tests involved a straight path and various initial conditions. The initial offset was 1 meter

from the track, and the heading offset was 10 and -10 degrees for the first and second tests, respectively.

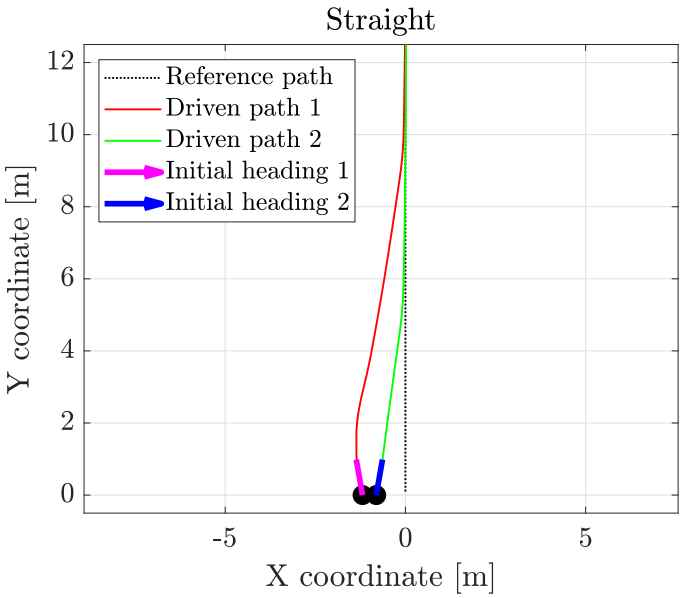

Figure 6.26: Straight path manuever

As shown in the figure 6.26, the path-tracking algorithm smoothly guides the vehicle back to the track. This behavior is a result of saturating the cross-track controller. If a faster response is needed, the saturation can be increased.

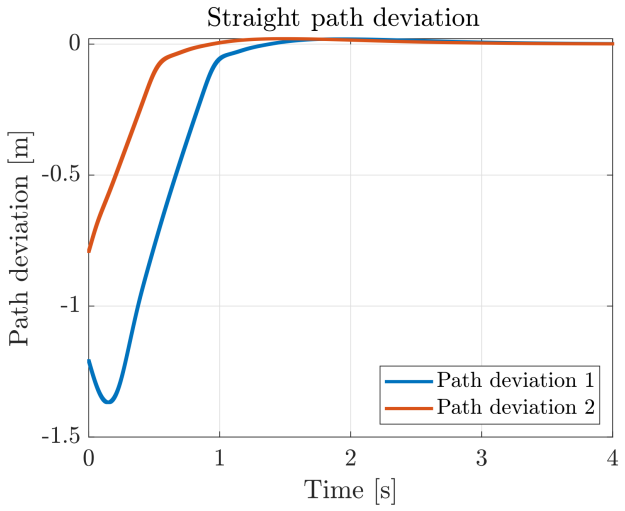

Figure 6.27: Straight path cross track error

6.2.3 S-Turn

The last experiment consisted of a S-turn, where the diameter matched the Skidpad track layout, thus the diameter is 16.25 meters. The test was done at two distinct velocities of 5 and 10 m/s.

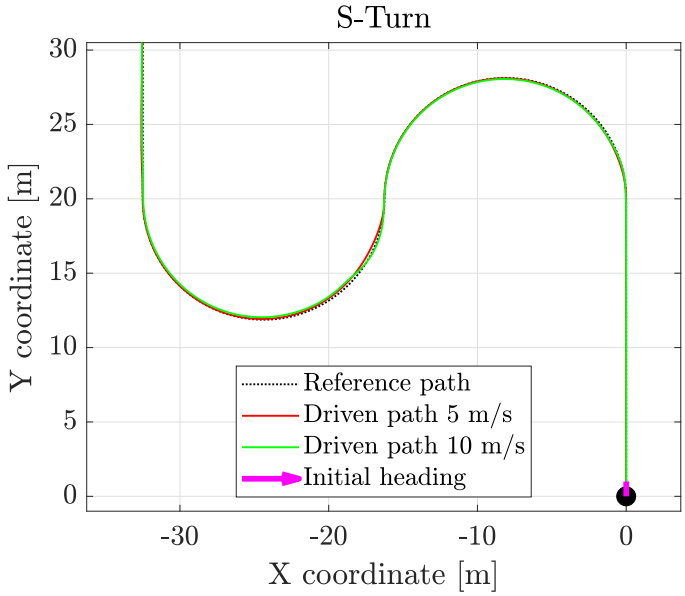

Figure 6.28: S-turn of 16.25 m diameter at a velocity of 5 and 10 m/s

Figure 6.29 demonstrates how path-tracking follows the reference heading.

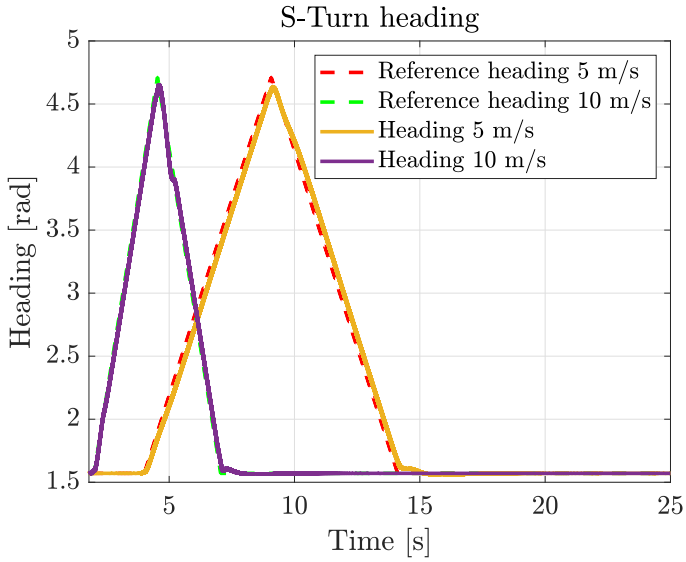

Figure 6.29: S-turn of 16.25 m diameter reference heading tracking

Figure 6.30 shows that the maximum deviations from the track occur at the point where the car passes through the center of the S-turn and when it

transitions to the straight or circular parts of the track. The cross-track error exceeds 0.2 meters at a velocity of 10 m/s, although it remains within the track boundaries. Similarly, for the tight U-turn, the controller should be tuned to be more aggressive in order to better handle the center transition.

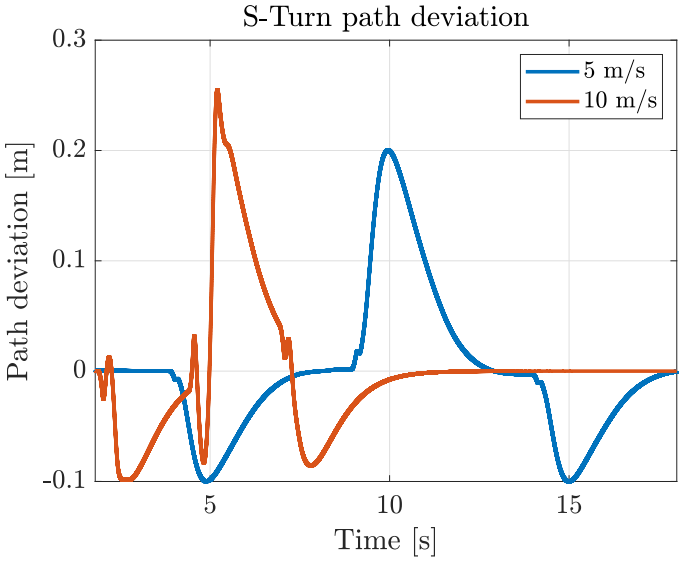

Figure 6.30: S-turn of 16.25 m diameter cross track error

It should be noted that the 10 m/s velocity is near the maximum feasible velocity for a turn with this diameter. Lastly, the figure 6.31 demonstrates the steering angle generated by the path-tracking.

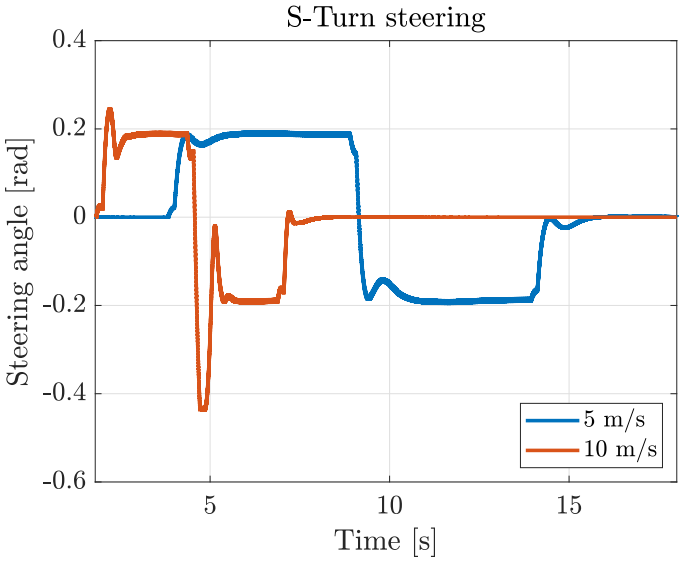

Figure 6.31: S-turn of 16.25 m diameter steering command

Chapter 7
Conclusion

7.1 Discussion

The aim of this thesis was to implement and validate vehicle dynamics control and path tracking for autonomous formula vehicle. The vehicle dynamics controllers functioned as intended. However, the overall vehicle dynamics control was limited by the wheel speed controller, which introduced small oscillations due to being designed for the fastest possible response. The remaining controllers work as intended, improving the autonomous formula's performance on the track in terms of vehicle dynamics.
The path-tracking algorithm demonstrates great performance when driving on the verification paths that simulate the competition tracks. The only non-ideal behavior is observed in turns with a small diameter, as the vehicle drives through them with a constant cross-track error. As the controllers can be specified for each of the disciplines, this issue is not significant.

7.2 Future work

Integration

The system developed in this thesis must be implemented into the autonomous system and integrated with the other algorithms used in the system.

Wheel speed controller

As previously mentioned, the wheel speed controller was not optimally tuned. Therefore, further analysis of the drivetrain and powertrain dynamics is necessary, as well as a newly tuned wheel speed controller to eliminate the unintended behavior. Additionally, the controller is intended to be directly implemented into the inverters.

Path-tracking

As demonstrated in this thesis, the designed path-tracking algorithm was sufficient for autonomous driving, although not ideal. Therefore, further

research on path-tracking algorithms is needed, Potentially experimenting with other control strategies, such as using the lookahead in a different way than in this thesis, to eliminate the cross-track error in tight turns.

Bibliography

[1] Formula Student Germany, "Formula Student," [Online]. Available: https://www.formulastudent.de/about/concept/, [Accessed: Dec. 27, 2023].

[2] FSG Maru, "Formula Student Germany Team Photo 2022," [Online]. Available: https://www.facebook.com/FSGeV/photos/a.493056594104904/5378789425531572/?type=3, [Accessed: Jan. 1, 2024].

[3] E. Alcalá, V. Puig, and J. Quevedo, "LPV-MPC Control for Autonomous Vehicles," *IFAC-PapersOnLine*, vol. 52, no. 28, pp. 106-113, 2019, DOI: https://doi.org/10.1016/j.ifacol.2019.12.356, [Accessed: Dec. 10, 2023].

[4] G. Hoffmann and C. Tomlin, "Autonomous Automobile Trajectory Tracking for Off-Road Driving," Stanford University, CS Department, 2007. [Online]. Available: http://robotics.stanford.edu/~gabeh/papers/hoffmann_stanley_control07.pdf, [Accessed: Dec. 10, 2023].

[5] M. Theers and M. Singh, "Pure Pursuit Algorithm," [Online]. Available: https://thomasfermi.github.io/Algorithms-for-Automated-Driving/Control/PurePursuit.html, [Accessed: Dec. 10, 2023].

[6] Robert Bosch GmbH, "Antilock Braking System," [Online]. Available: https://www.bosch-mobility.com/en/solutions/driving-safety/antilock-braking-system/, [Accessed: Dec. 24, 2023].

[7] National Safety Council, "ABS Functionality Illustration," 2023, [Online]. Available: https://mycardoeswhat.org/safety-features/anti-lock-braking-system/, [Accessed: Dec. 24, 2023].

[8] Robert Bosch GmbH, "Electronic Stability Control," [Online]. Available: https://www.bosch-mobility.com/en/solutions/driving-safety/electronic-stability-program/, [Accessed: Dec. 24, 2023].

[9] Care For Your Car, "ESP Functionality Illustration," 2022, [Online]. Available: https://careforyourcar.co.uk/what-is-traction-control/, [Accessed: Dec. 24, 2023].

[10] Kia Corporation, "Traction Control System," [Online]. Available: https://www.kia.com/dm/discover-kia/ask/what-is-the-traction-control-system-in-a-car-and-what-does-the-tcs-light-me html, [Accessed: Dec. 24, 2023].

[11] Bugatti Rimac d.o.o., "All Wheel Torque Vectoring," [Online]. Available: https://www.rimac-automobili.com/media/press-releases/rimac-all-wheel-torque-vectoring/, [Accessed: Dec. 24, 2023].

[12] Tesla, "Lateral Torque Vectoring," [Online]. Available: https://www.tesla.com/blog/introducing-plaid-track-mode, [Accessed: Dec. 24, 2023].

[13] UNMANNED SOLUTION R&D Team, "INS Ellipse2-D," SBG Systems, [Online]. Available: https://www.sbg-systems.com/case-studies/ins-gnss-autonomous-navigation, [Accessed: Dec. 19, 2023].

[14] Maxon, "220W Brushless DC Motor," [Online]. Available: https://www.maxongroup.com/maxon/view/product/motor/ecmotor/ecflat/ecflat90/607942?target=articleDetail, [Accessed: Dec. 20, 2023].

[15] RLS, "Absolute Rotary Encoder," [Online]. Available: https://www.rls.si/media/catalog/product/m/h/mhad01_10__en_data_sheet_.pdf, [Accessed: Dec. 20, 2023].

[16] IPG Automotive, "CarMaker," [Online]. Available: https://ipg-automotive.com/en/products-solutions/software/carmaker/.

[17] eForce Prague Formula, "eForce Prague Formula," [Online]. Available: https://eforce.cvut.cz/, [Accessed: Dec. 15, 2023].

[18] Denis Efremov, "Wheel Coordinate System," [Online]. Available: https://gitlab.fel.cvut.cz/hanistom/VehicleModel/-/blob/master/reports/single-track/FullModel/SingleTrackModelDerivation.pdf, [Accessed: Oct. 10, 2023].

[19] H. Pacejka, *Tire and Vehicle Dynamics*, Netherlands: Elsevier Science & Technology Books, 2012.

[20] D. Schramm et al., *Vehicle Dynamics: Modeling and Simulation*, Německo: Springer Berlin Heidelberg, 2017.

[21] R. Rajamani, *Vehicle Dynamics and Control*, United Kingdom: Springer US, 2011.

[22] The MathWorks, Inc., "atan2 Function," [Online]. Available: https://www.mathworks.com/help/matlab/ref/atan2.html, [Accessed: Oct. 5, 2023].